FRAGMENTATION OF RELATIVISTIC LIGHT NUCLEI: LONGITUDINAL AND TRANSVERSE MOMENTUM DISTRIBUTIONS

Leonard M. Anderson, Jr.

ABSTRACT

We have measured the production of charged nuclear fragments in collisions of 0.93 GeV/c/nucleon, 1.75 GeV/c/nucleon, and 2.88 GeV/c/nucleon alpha particles on targets of carbon, copper, lead, and CH_2, using a double focusing spectrometer. We present single particle inclusive cross sections for the production of protons, deuterons, tritons, ^3He, and ^4He at momenta from 0.5 to 11.5 GeV/c and angles from 0° to 12°. We discuss the relevance of the concept of limiting fragmentation to our data and point out possible uses of the data to study nuclear structure and particle production mechanisms.

ACKNOWLEDGEMENTS

The scale of this experiment was such that it is only through some extraordinary efforts by some extraordinary people that I have been able to survive (and, amazingly, even enjoy) the whole thing. So my greatest pleasure in writing this thesis is this opportunity to thank those people who have guided my education, stimulated my interest and curiosity with their questions, helped me with their physical and mental labor, and warmed and cheered me with their support and friendship. Owen Chamberlain, Herbert Steiner, and Gilbert Shapiro have through their leadership and example made the Segrè-Chamberlain Group a challenging and friendly place in which to work and learn. Owen's experience, intuition, and careful thought continue to amaze me and have guided me through many of the crucial turns in this experiment. Herb inspired, encouraged, criticized, and drove me to and through this venture, and his energy will always be an example to me. Gil, with considerable speed and dexterity, put the on-line analysis program together, and his helpful suggestions and stimulating conversations will long be remembered.

Sven Nissen-Meyer was my right hand throughout most of this project. Without his ideas, hard work, friendship, and support it would have been impossible, and without his persistent but innocent questions, the left hand often wouldn't have known what it was doing. Lee Schroeder provided much of the original stimulus for this experiment, and his continued interest and support and his successful infiltration of the Bevalac scheduling staff were invaluable. Shoji Nagamiya contributed very generously his effort and talent in measuring, parameterizing and trying

to control the too many magnets in this experiment. David Nygren did a fine job of designing and putting together the target system. John Jaros, Gary Godfrey, Walter Brückner, Isao Tanihata, Marcel Urban, Steve Schnetzer, Craig Blocker, Jeff Tennyson, Jim Eisenstein, Mark Eaton, and Jim Wiss lent their able hands to the design, construction, and running of the apparatus. Thanks also go to Mark Coles for bringing the hot chocolate.

Ray Fuzesy taught me all I know about machinery, built the wire chambers and, in spite of our best efforts, tried to keep them clean, and warned me of more road hazards than I can remember.

I shall be forever grateful to Jeff Gallup who worked under tremendous pressure to build a very fast and flexible data acquisition system. Jeanne Miller typed this thesis with wondrous speed and cheer, and the sound of her delightful laughter ringing in the hallway is as essential here as are the birds in the forest. Barbara Ockel--what can I say? She tended a hundred terrible tapes, launched a thousand lovely plots and brought countless smiles that carried me through my darkest hours and brightened my brightest days.

I would also like to thank Hermann Grunder and the many fine people at the Bevalac, George Constantian and the folks at the equipment pool, Jim Harvill and the computer support staff, and Frank Porter, the Ergon man, for their generous help.

I feel great love and gratitude toward my parents for their understanding, care, and support over these long years. I thank my roommates and friends for their much-needed friendship and their tolerance of my

absence, and I thank all those with whom I have talked about physics for their company in being as awed and mystified by Nature as I am.

Work performed under the auspices of the U. S. Department of Energy under Contract W-7405-ENG-48.

TABLE OF CONTENTS

Acknowledgements i

I. Introduction 1

II. Theory and Phenomenology 5

A. The Single Particle Inclusive Cross Section 5

B. Kinematics 6

C. Limiting Fragmentation 9

III. Experimental Method 14

A. Primary Beam 14

B. Targets 14

C. Primary Beam Monitors 19

D. Spectrometer 22

E. Particle Detection and Identification 26

F. Electronics 30

G. Running Plan 32

IV. Data Analysis 35

A. Particle Identification 35

B. Calculation and Normalization of Cross Sections 46

C. Corrections to the Data 50

D. Sources of Error 50

E. Editing of the Data 55

V. Results and Conclusions 58

A. General Characteristics 60

B. Limiting Fragmentation 84

C. Projectile Frame Anisotropy 89

D. Target Dependence..... 95

E. Model Comparison.....103

F. Summary and Conclusion.....117

References.....119

Appendices

I. Ionization Chamber Calibration.....122

II. Monitor Telescope Calibrations.....125

III. Acceptance Calibration.....127

I. INTRODUCTION

The acceleration of nuclei to relativistic velocities at the Bevatron/Bevalac has made it possible to study nucleus-nucleus reactions in a new and higher energy domain. We have carried out a survey experiment using beams of protons, deuterons, alpha particles and carbon nuclei with kinetic energies of 0.4, 1.05, and 2.1 GeV per nucleon, measuring the yield of charged particles in the near forward direction over a wide range of momenta and yielding cross sections spanning 10 orders of magnitude. This thesis reports the results of the measurements made with the alpha particle beams.

The study of hadronic matter traditionally has been carried out by two separate groups of researchers studying two separate areas, divided apparently according to the baryon number of the systems being studied: "Elementary particle physics" (B = 0 and 1), and "nuclear physics" (B ≥ 2). Chew has argued that according to the concept of "nuclear democracy" the same strong interaction characteristics are responsible for the existence and behavior of all hadrons and that this distinction should be abandoned.[1,2] He has also conjectured that, whenever the energy available in a collision is much greater than the energy levels of the excited states of the hadrons involved, then "high energy" or asymptotic behavior may arise which would make evident the composite nature of the hadrons involved.[3] Part of the interest in nucleus-nucleus reactions at these "high" energies of 1-2 GeV/N was thus stimulated by questions as to whether they would exhibit "high energy" behavior similar to that observed in proton-proton interactions at hundreds of GeV.

This behavior is expected since the kinetic energy of the colliding nucleus (1 GeV/N) is much greater than its excited state energy levels and binding energy (8 MeV/N), just as the energy in high energy proton-proton scattering (100 GeV) is much greater than the energies of the excited states of the proton (i.e. the resonances near 1 GeV). In particular, one of the most prominent features of nucleus-nucleus collisions in this energy range is the existence of strong peaks in the production of nuclear isotopes of masses less than that of the projectile observed close to the velocity of the projectile.[4-7] These products are widely interpreted as fragments of the projectile nucleus. According to the hypothesis of limiting fragmentation,[8] which has been shown to have considerable validity in high energy elementary particle interactions,[9] the momentum distributions of these fragments in the projectile Lorentz frame should be independent of beam energy and target material. One of the chief aims of this experiment is to determine the degree and range of validity of this hypothesis and, we hope, to provide enough data to allow a determination of its physical basis.

As one extreme form of interpretation, we might assume that the fragmentation process disturbs the wave function of the projectile so minimally that the fragment momentum distributions in the projectile frame are isotropic and are determined solely by the momentum-space wave functions of the projectile nucleus.[10] More plausibly, perhaps it is possible to construct models incorporating the wave function and nucleon-nucleon scattering, for example, applying the successful approach of Glauber's multiple scattering theory[11] to explain these fragment

momentum distributions or to extend our knowledge of nuclear wave functions. Models of this nature have been constructed to describe the breakup of deuterons.[12,13] Other Glauber theory-based models have been proposed to describe the fragmentation of heavier projectile nuclei.[14,15]

Models of elementary particle structure have been developed which employ pointlike constituents called "partons"[16] and predict "scaling," namely that for high enough projectile energies the distribution of particles in the available longitudinal phase space is independent of beam energy. Of course, nuclei are known to be composed of nucleons and, although nucleons are not pointlike, it may be that parton models are relevant to understanding high energy nucleus-nucleus collisions. In fact, scaling has been observed in the production of pions in this energy range[4] and parton models have been advanced to predict the fragment momentum distributions.[17,18] Other models predicting these distributions employ statistical ideas[19,20] and Monte Carlo simulation of cascades from nucleon-nucleon collisions.[21-24]

Correpsonding to the projectile fragmentation region, there is a target fragmentation region of products characterized by low velocity in the laboratory.[25] And, at velocities intermediate between the target and projectile, there is a central region[26-29] to which additional methods have been applied.[30-39]

It is the spirit of Chew's injunction that hadron physics will benefit considerably from an exploration of the underlying unity of "elementary particle physics" and "nuclear physics."[1] The joining of relativistic treatment and the high energy techniques for the study

of particle structure, together with what is already known about nucleon-nucleon forces and nuclear structure, will, we hope, provide new insight into the high energy concepts and new information about the interaction among nucleons in the nucleus, especially at short ranges.

This experiment was designed and carried out with these questions in mind; the fact that the projectile fragments into particles in a narrow forward cone with momenta easily measurable in the laboratory allows us to measure the momentum distributions of these fragments in the projectile frame in the forward, backward, and transverse directions; in some cases from 0 to 600 MeV/c/N. In addition, we are able to get some measurements of the tail of the target fragmentation region and cover the central "plateau" region of intermediate velocities.

II. THEORY AND PHENOMENOLOGY

A. The Single Particle Inclusive Cross Section

We have measured cross sections for reactions of the form

$$a + b \rightarrow c + \text{anything}.$$

The relevant cross section is the area for producing a particle in an infinitesimal volume of the single particle Lorentz invariant phase space

$$\frac{d^3\sigma^c_{ab}}{d^3\vec{p}/E} = E\frac{d^3\sigma^c_{ab}}{d^3\vec{p}}(s,\vec{p}) = \frac{E}{p^2}\frac{d^2\sigma^c_{ab}(s,\vec{p})}{d\Omega dp}$$

where E and $\vec{p}$ are the energy and momentum of particle c and s is the square of the energy of the entire system in the center of mass. This is called the Lorentz invariant single particle inclusive cross section, or simply, the invariant cross section.

Another form commonly used is the cross section in the laboratory frame

$$\frac{d^2\sigma^c_{ab}}{d\Omega dp}(s,\vec{p})$$

which is the form most directly calculated from the experimental raw data. The cross section is determined by counting the number of beam particles N_a incident on a target containing n_b target nuclei per unit area, and the number of particles N_c of type c produced into a solid angle-momentum volume $\Delta\Omega\Delta p$ centered about momentum p. The laboratory cross section is then

$$\frac{d^2\sigma^c_{ab}}{d\Omega dp} = \frac{N_c}{N_a}\frac{1}{\eta_b}\frac{1}{\Delta\Omega\Delta p} .$$

B. Kinematics

There are several sets of variables that are relevant for the study of inclusive reactions. Since our beams and targets did not have polarized spins, the cross section should be independent of azimuthal angle, i.e. it depends only on the components of the momentum of the produced particle parallel (p_L) and transverse (p_T) to the direction of the incident projectile

$$E\frac{d^3\sigma}{d^3\vec{p}}\ (s, p_L, p_T).$$

For describing projectile fragmentation it is useful to use the variables in the projectile frame, p_L^{PROJ} and p_T.

Another very useful variable is the rapidity, defined as

$$y = \frac{1}{2}\ln\frac{E+p_L}{E-p_L} = \tanh^{-1}\frac{p_L}{E} .$$

Under a Lorentz boost transformation in the longitudinal (beam) direction, the rapidity transforms additively, so that rapidity distributions are independent of the Lorentz frame. At $p_T = 0$, we have $y = \tanh^{-1}\beta$, so the rapidity is essentially a velocity variable. Hence the projectile fragment rapidity distributions peak near the projectile rapidity, and the target fragments peak near $y = 0$. The rapidity distribution thus shows us what reference frame is relevant for describing a given process.

Also useful are the longitudinal and radial scaling variables

$$x' = \frac{p_L^{CM}}{p_{MAX}^{CM}}, \quad \text{and} \quad x_R = \frac{p^{CM}}{p_{MAX}^{CM}}$$

where p^{CM} is the momentum in the center-of-mass frame, p_L^{CM} is its longitudinal component, and p_{MAX}^{CM} is the maximum momentum in that frame for the given reaction.

Some of the relationships between these variables should be pointed out. Because the rapidity transforms additively under Lorentz boosts, any distribution which is limiting (i.e. independent of projectile energy at high enough energy) in p_L^{PROJ} and p_T will be limiting in y and p_T. However, in contrast with high energy proton-proton scattering, limiting fragmentation does not imply scaling (energy independence of the x' distribution). Fig. 1 shows the relationships between p_L^{PROJ} and x' for 0.93, 1.75, and 2.88 GeV/c/N $\alpha + c \rightarrow p + X$ at $\theta = 0°$. Clearly limiting fragmentation and scaling are inconsistent at these energies where the masses of the particles involved are not negligibly small relative to the projectile energy.

We conclude this section with Table 1 which lists some of the kinematic parameters for the three energies of alpha beams used in the experiment. We tabulate the beam's momentum per nucleon, kinetic energy per nucleon, velocity $\beta_B = v/c$, $\gamma_B = (1 - \beta_B^2)^{-1/2}$, rapidity, and the laboratory momentum at which each fragment would have zero momentum in the projectile frame.

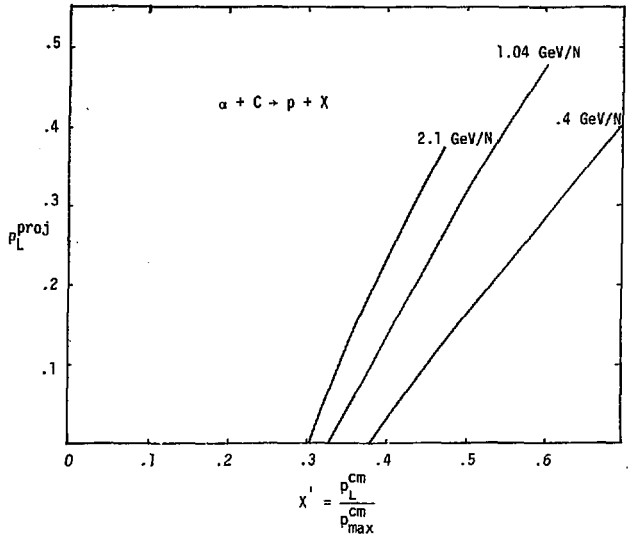

Fig. 1. p_L^{proj} vs x' for the reaction α+C→p+X at the three alpha beam energies used in this experiment.

Table I. Some kinematic parameters for the three alpha particle beam energies used in this experiment.

P/N (GeV/c)	T/N (GeV)	β	α	Expected peak momentum (GeV/c) proton	deuteron	$^3H, ^3He$	alpha
0.93	0.39	0.707	1.41	0.93	1.87	2.80	3.72
1.75	1.04	0.882	2.12	1.75	3.50	5.25	7.0
2.88	2.09	0.951	3.24	2.88	5.76	8.66	11.5

XBL 779-2468

C. Limiting Fragmentation

Studies of inclusive reactions in high energy pp collisions and in heavy ion collisions at 1-2 GeV kinetic energy/nucleon have shown three similarities:

1) limited transverse momentum: the cross section falls very steeply with transverse momentum;[5]
2) persistence of velocity, or leading particle effect--the invariant cross section is peaked at or slightly below the projectile rapidity. In nucleus-nucleus collisions this holds for the baryonic products of mass less than the projectile nucleus;[5] in proton-proton collisions it holds for the inelastic inclusive proton and baryon resonance production;
3) approximately constant total cross section and inelastic cross section.[40]

These facts are consistent with an intuitive picture of the dominant collision process in which the projectile breaks up under the influence of the target, and the target breaks up under the influence of the projectile, yielding products moving slowly in the respective rest frames of the fragmenting nuclei.

This picture is defined more precisely in the hypothesis of limiting fragmentation which states that the invariant cross section is limiting, i.e. that the limit

$$\lim_{s\to\infty} E \frac{d^3\sigma^c_{ab}(s,p_L,p_T)}{d^3p} = \rho_b(p_L,p_T)$$

exists over a finite range in p_L and p_T near 0. Particles produced in this range are identified as fragments of the target b. Similarly, there is a limiting distribution of projectile fragments which have finite momenta in the projectile frame:

$$\lim_{s\to\infty} E \frac{d^3\sigma^c_{ab}(s, p_L^{PROJ}, p_T)}{d^3\vec{p}} = \rho_a(p_L^{PROJ}, p_T).$$

The projectile energy range over which we may expect to see approximate limiting behavior is determined by two factors: 1) The projectile kinetic energy per nucleon must be much greater than the binding energies per nucleon of the target and projectile. 2) The projectile rapidity must be great enough so that the fragment distributions of the target and projectile do not overlap. As we have mentioned earlier, condition (1) is well satisfied for nuclei at 1 GeV/N. The rapidity of a projectile at 1.05 GeV/N (1.75 GeV/c/N momentum) is 1.4, while the width of the rapidity distribution for protons is approximately 0.2, so condition (2) is also met.

Thus we may expect the single particle inclusive cross sections to show approximate limiting behavior (energy independence) at 1-2 GeV/N. This may be so even though the limits defined in (1) and (2) do not exist or are quite different from the value of the cross section at 1 GeV/N. Above this energy range where the structure of the nucleons begins to influence the production cross sections (through resonance and multiparticle production) there may be a transition region of energy dependence to the higher energy asymptotic region where the substructure of the individual nucleons is exhibited as well as the nuclear substructure.

Limiting fragmentation may be implied by several different physical pictures of the collision process. Perhaps the simplest of these is expressed in the sudden approximation which has been applied to projectile fragmentation by Lepore and Riddel.[10] The wave function of the projectile nucleus is assumed to be changed negligibly during the collision so that the amplitude for a given final state is simply the overlap integral of that final state with the intitial state. The result is that the projectile frame momentum distribution is isotropic and straightforwardly obtained from the momentum space wave function after imposing momentum conservation. Such a model clearly implies limiting fragmentation.

We may make a less strict set of assumptions and include the effects of the scattering of the nuclei if we use the framework of Glauber multiple scattering theory.[11] This theory in simplest approximation treats each nucleus as a collection of independent on-mass-shell nucleons. During the collision the nucleons within each nucleus are assumed to have constant velocity and not interact with each other. The total scattering phase shift is taken to be the sum of the individual nucleon-nucleon scattering phase shifts. Such a model for the reaction d + target → p + X has been proposed by Bertocchi, Tekou, and Treleani[12] and refined by Nissen-Meyer,[13] who calculates the diagrams in Fig. 2 and whose results agree with the existing data over most of the momentum range in which agreement is expected. Such a model will predict limiting fragmentation when the nucleon-nucleon total cross section is energy-independent--as it is in the energy range 1-2 GeV/N.

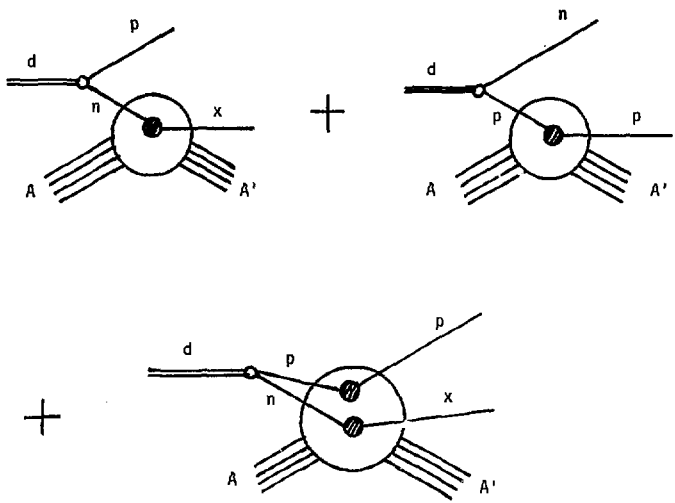

XBL 779-2465

FIg. 2

Other models may be constructed using entirely different physical pictures to predict the fragment momentum distributions. The value of the hypothesis of limiting fragmentation is that it serves as a criterion for determining the projectile energy necessary and the momentum range over which the distributions may be taken to reflect the structure of the fragmenting nucleus. Then, with the help of models incorporating the dynamics of the fragmentation process, we can perhaps learn more about the details of that structure.

III. EXPERIMENTAL METHOD

The apparatus consisted primarily of a single arm double focusing spectrometer which transported the particles produced in the targets to our detectors and provided momentum analysis and production angle selection. The particles were detected by scintillation counters and identified by measurement of magnetic rigidity, time-of-flight, and dE/dx. The data were recorded by an on-line PDP-11 computer on magnetic tape.

A. Primary Beam

Primary beams of alpha particles at 0.93, 1.75, and 2.88 GeV/c/nucleon were obtained from the Bevatron External Particle Beam and transported to the target in the beam line shown in Fig. 3. Quadrupoles X1Q5A and X1Q5B focused the beam at F3 10 meters downstream from the target, producing at the target an elliptical beam spot with a horizontal axis of 10 cm and a vertical axis of 5 cm containing about 98% of the beam. Beam intensities used varied from a few thousand per pulse up to the maxima available: 3×10^9 alpha particles for a pulse of 0.5 to 1.2 seconds. Beam contamination was minimized by a putting a minimum amount of material in the beam line, by continuously monitoring the centering of the beam with wire chambers, and by attenuating the beam from the source before injection to obtain lower operating intensities.

B. Targets

The targets used in the experiment are listed in Table 2, along with some of their properties. The principal targets used were the "standard"

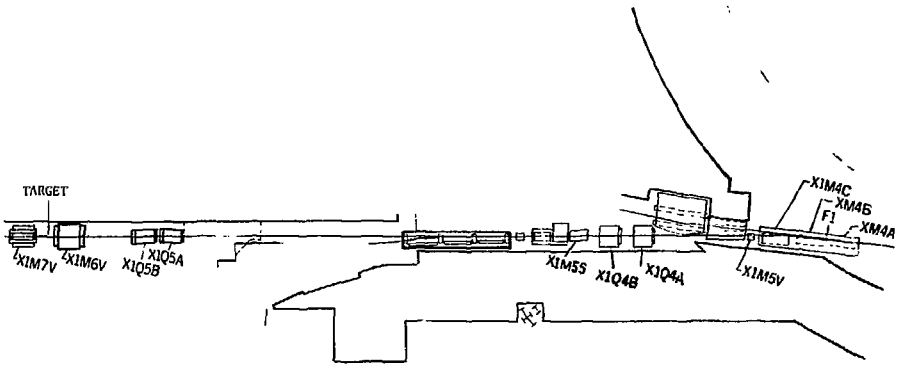

Fig. 3

Bevalac External Particle Beam Channel 1.

The Primary Beam Transport System used to deliver the alpha beams to our targets.

carbon, copper, lead, CH_2, and empty targets. The targets were mounted on aluminum holders connecting two stainless steel bicycle chains, as shown in Fig. 4. The chains were driven by a computer controlled electric stepping motor, allowing the targets to be raised or lowered in steps of .01 inch.

The principal targets were of identical size transverse to the beam axis. They were hexagons which approximate an ellipse with axes of 11.3 cm horizontally and 5 cm vertically so that they would intercept approximately 98% of the beam. The target holders were also identical, and the empty target was one of the holders with no target mounted in it. The sizes and shapes of the targets are shown in Fig. 5.

The "thin" carbon target was used to determine effects of target thickness. The "small" and "large" targets had differing dimensions transverse to the beam axis, allowing us to check whether the transmission of the spectrometer was different for different regions of the target. The "large" targets were used to calibrate some of the beam monitors, as will be explained in Appendix II.

The surfaces of the targets were machined plane and their thicknesses measured with a micrometer and their density determined by weight and by measurement with a micrometer. From this we determined the number of nuclei per unit area $n = N_0 \rho \ell / A_T$ where N_0 is Avogadro's number, $\rho\ell$ is the thickness in gm cm^{-2}, and A_T is the atomic weight. For the CH_2 target, this number refers only to the hydrogen component of the target.

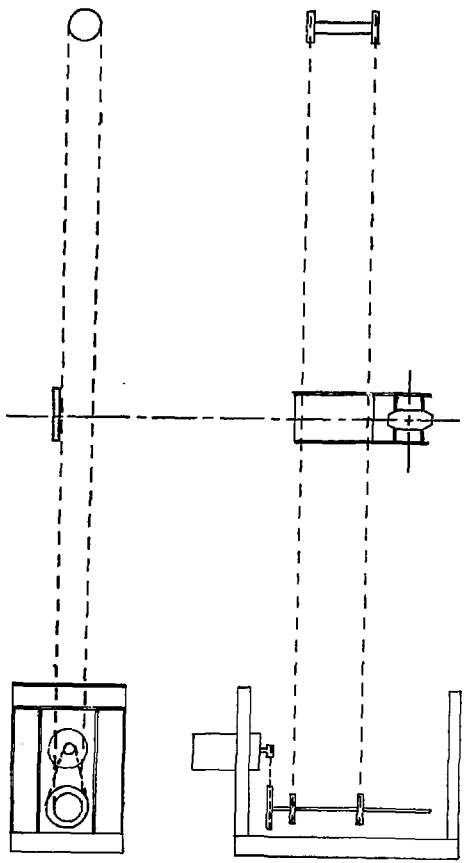

XBL 779-2441

Fig. 4

TARGET MECHANISM

Table 2. List of targets used in the experiment along with their thickness in cm. and in gm./cm.^{2}, and the number of nuclei per unit area.

TARGET	ℓ (cm.)	$\rho\ell$ (gm./cm.^{2})	n (nuclei/mb.)
C	1.267	2.302	$1.154 \pm .009 \times 10^{-4}$
Cu	.3409	3.005	$2.848 \pm .024 \times 10^{-5}$
Pb	.6834	7.696	$2.237 \pm .017 \times 10^{-5}$
CH_2 (H)	2.568	2.355	$2.022 \pm .016 \times 10^{-4}$
LARGE C	1.270	2.233	$1.120 \pm .008 \times 10^{-4}$
LARGE Cu	.3327	2.947	$2.793 \pm .022 \times 10^{-5}$
LARGE Pb	.6828	7.853	$2.283 \pm .018 \times 10^{-5}$
LARGE CH_2 (H)	2.172	2.007	$1.723 \pm .014 \times 10^{-4}$
SMALL C	1.267	2.281	$1.144 \pm .009 \times 10^{-4}$
THIN C	.6453	1.431	$5.669 \pm .045 \times 10^{-5}$

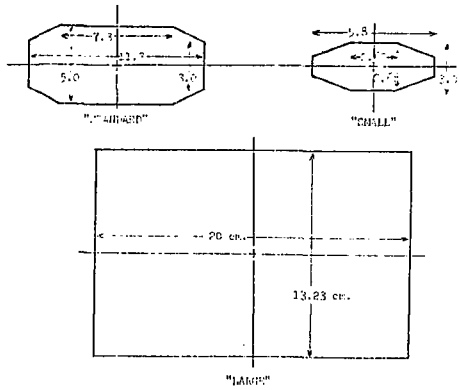

Fig. 5. Dimensions of the "standard", "small", and "large" targets (cm.).

C. Primary Beam Monitors

The position and profile of the primary beam was monitored with a wire chamber mounted in the beam line 1.9 m upstream of the target. The charge collected on each of the 32 wires of the 19.2 cm by 19.2 cm chamber was integrated on a pulse-by-pulse basis, allowing continuous monitoring via an oscilloscope display of the profile thus obtained in both horizontal and vertical directions.[41]

The six beam intensity monitors are listed in Table 3, along with the sensitivities for the various beams. B is a scintillation counter placed in the beam line to count the beam particles directly at low intensities.

The ionization chamber (IC) and the secondary emission monitor (SEM) were also mounted in the beam line upstream of the target. Each was connected to an electrometer and capacitor. The voltage across the capacitor was read into the computer by a digital voltmeter before and after the beam pulse. The calibration of the IC is described in Appendix I.

Scintillation counter telescopes M1, M2, and M3 are diagrammed in Fig. 6. They each consist of 3 scintillation counters connected in coincidence and aligned so as to be sensitive to particles coming from the direction of target. Special care was taken in the design of the sizes and placement of the counters to insure that they would be sensitive to the entire target and not to other possible sources of particles and to insure that only one of the 3 counters determines the solid angle of the coincidence. The telescopes then provide a relative measure of the

Table 3. Beam monitor calibration constants in units of incident alpha particles per monitor count. For the ionization chamber (IC) and the secondary emission monitor (SEM) 1 count = 10 picocoulombs. For M1, M2, and M3 the numbers are given for the "standard" carbon target. For M3 the calibration applies at 0°. Typical errors are ±2%.

Monitor	0.93 GeV/c/N	1.75 GeV/c/N	2.88 GeV/c/N
B	1.00	1.00	1.00
IC	2.64×10^{5}	3.60×10^{5}	3.82×10^{5}
SEM	5.32×10^{7}	7.52×10^{7}	7.85×10^{7}
M1	6.06×10^{4}	2.05×10^{4}	1.41×10^{4}
M2	6.32×10^{7}	1.96×10^{7}	1.04×10^{7}
M3	4.99×10^{5}	2.11×10^{5}	1.44×10^{5}

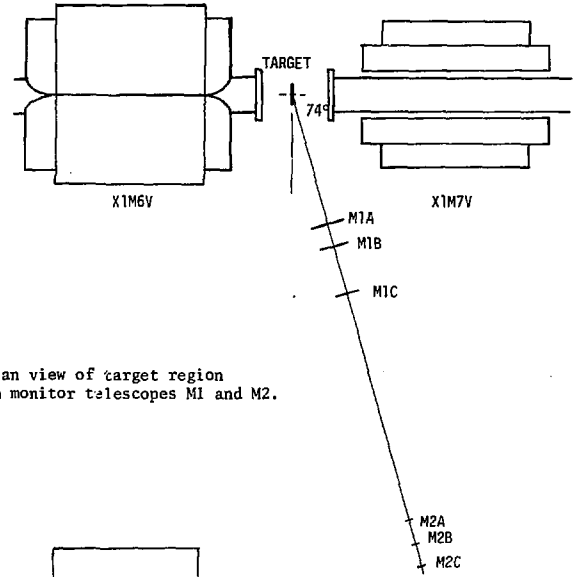

Fig. 6a. Plan view of target region showing beam monitor telescopes M1 and M2.

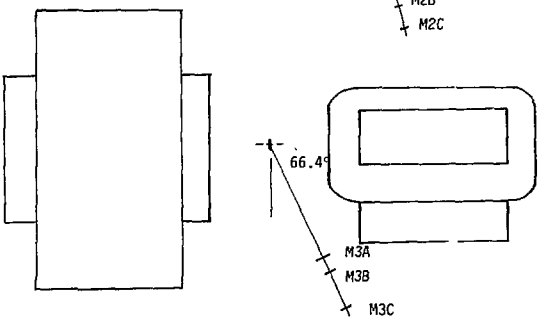

Fig. 6b. Elevation view of target region showing beam monitor telescope M3.

XBL 779-2455

intensity of the beam incident on the target by counting particles produced in the target at large angles. The calibration procedure for the telescopes is described in Appendix II.

D. Spectrometer

The secondary particles produced in the target were momentum analyzed and transported to the detectors by Bevalac Beam 37, a double-focusing spectrometer consisting of 16 magnetic elements. The layout of the spectrometer is shown in Fig. 7.

Production angles between 0° and 12° were selected by setting the current in vertical bending magnets M6V and M7V. As shown in Fig. 8, M6V bent the primary beam upward by angle $\theta/2$. Particles produced in the target downward at angle θ are bent upward through angle $\theta/2$ by M7V to be parallel with the beam line. The target, of course, is placed at the proper height to intercept the primary beam.

The secondary particles were momentum dispersed and steered to a focus at F3 by horizontal bending magnets M8A and M8B. At F3 a 61 cm long uranium collimator was used to eliminate particles having magnetic rigidity more than 8% different or production angle 17 mr different from the central rigidity and angle to be detected. Additional momentum dispersion is provided by magnets M1A and M1B, and F3 is imaged at F4 by quadrupoles Q3 and Q4. The momentum dispersion is removed by magnets M2A and M2B, and F4 is imaged at F5 by Q7 and Q8. Quadrupoles Q1 and Q2 and Q5 and Q6 are used to contain the size of the beam envelope in the regions of F3 and F4 respectively, and to make the magnifications, and

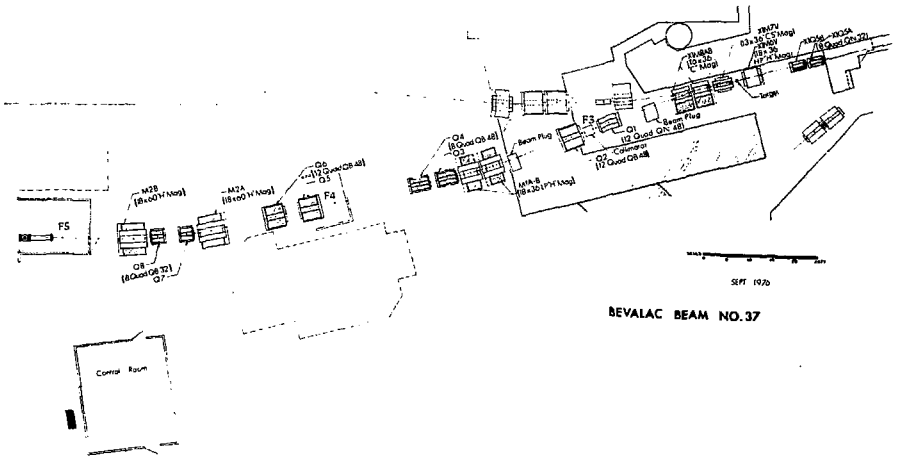

XBL 779-2456

Fig. 7. Beamline spectrometer used in this experiment. The detectors are located at focus points F4 and F5.

thus the acceptance of the spectrometer, stable with respect to small changes in the settings of the other quadrupoles. Q1/2 and Q5/6 image the target at the centers of quadrupoles Q3/4 and Q7/8, respectively. The acceptance stability was verified by remeasuring particle production at a given angle and rigidity setting, but with slightly different quadrupole settings.

In order to obtain the best possible angular resolution, we used the geometry shown schematically in Fig. 9. The primary beam is focused through the target to F3 so that the position of a secondary particle at F3 indicates the production angle. Since F4 and F5 are images of F3, they also have this angle information.

The spectrometer was designed with the aid of program TRANSPORT. The line integral field and field gradients as a function of current for the dipoles and quadrupoles, respectively, were measured using a long flip coil and current integrator. These results were then parameterized simply so that we could determine the proper currents to obtain any field integral within range. The magnet power supplies were computer controlled using an ADC-DAC closed loop feedback system. The optimum current settings were determined by transporting Bevatron primary beams of rigidity 1.75, 3.5, and 5.76 GV/c and centering and focusing the beam with the aid of multiwire proportional chambers placed at the target and foci F3, F4, and F5. The parameterizations allowed us to extend these optimum settings to any rigidity and were stored in the computer, so that we could change the rigidity and angle setting in a matter of seconds. The method of the calibration of the acceptance is described in Appendix III.

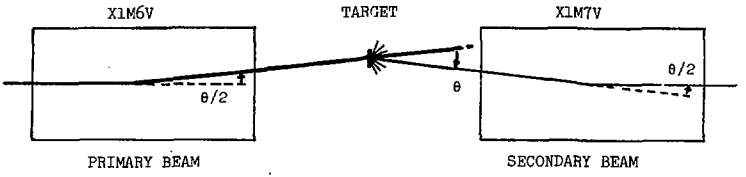

Fig. 8. Production angle selection method.

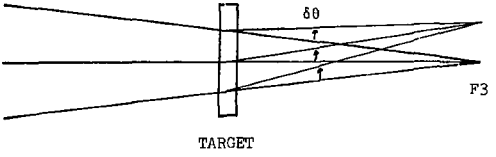

Fig. 9. Geometry used to obtain maximum angular resolution.

XBL 779-2443

E. Particle Detection and Identification

The charge and mass of the secondary particles detected were determined by a measurement of the magnetic rigidity (p/z), rate of energy loss (dE/dx), and time-of-flight (TOF). The rigidity and production angle were determined by scintillation counter hodoscopes located at F4 and F5. The dimensions and orientations of the counters are indicated in Fig. 10, and the approximate rigidity and angle regions covered by them are shown in Fig. 11. Information on energy loss was obtained by recording the pulse heights in the hodoscopes and in a 1/2" thick scintillator, called PH, which was viewed by four phototubes. The signals from the opposing pairs were added electronically to obtain signals nearly independent of where in the scintillator the particle passed through. These pulse heights and the pulse heights in the hodoscopes were recorded to give us five (four independent) measurements of energy loss rate for each event.

The particle velocity was determined from the time-of-flight along the 18 m path between the F4 and F5X hodoscopes. The F4 phototubes view their scintillators from above, while the F5X phototubes view their scintillators from below, so that, since the particle position at F4 is imaged at F5, the time-of-flight signal recorded is independent of particle position in the scintillators.

Fig. 12 is a scatter plot of the summed pulse height of two of the opposing phototubes looking at the PH scintillator versus the time-of-flight. The separation of p, d, ^{3}He, and ^{4}He is clearly indicated. These scatter plots, as well as the time-of-flight and pulse height distributions in all the counters were available in the on-line computer,

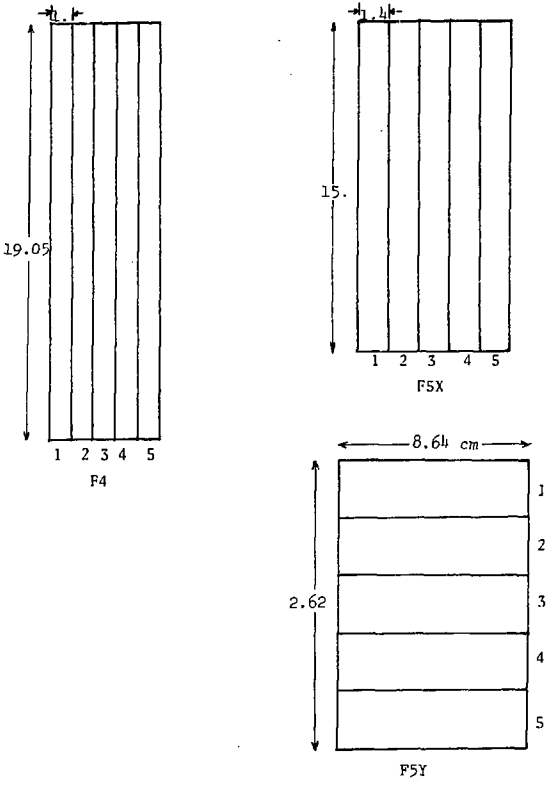

Fig. 10. Beam's eye view of the hodoscopes (cm., 1/2 scale).

XBL 779-2444

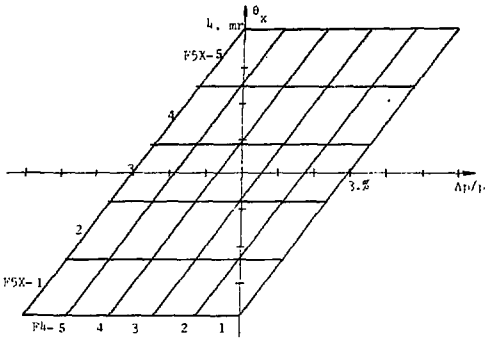

Horizontal plane

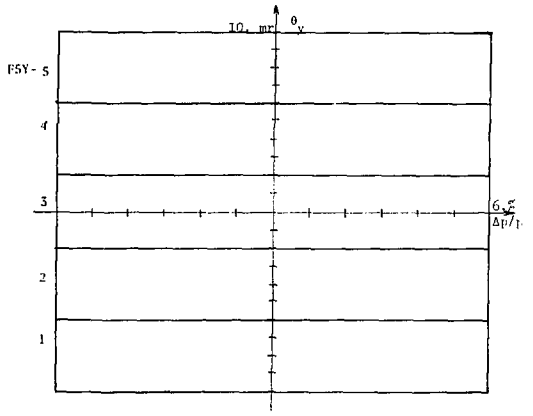

Vertical plane

Fig. 11. Approximate hodoscope acceptance regions in angle θ and relative momentum $\Delta p/p$, according to first order beam optical transport theory.

XBL 779-2445

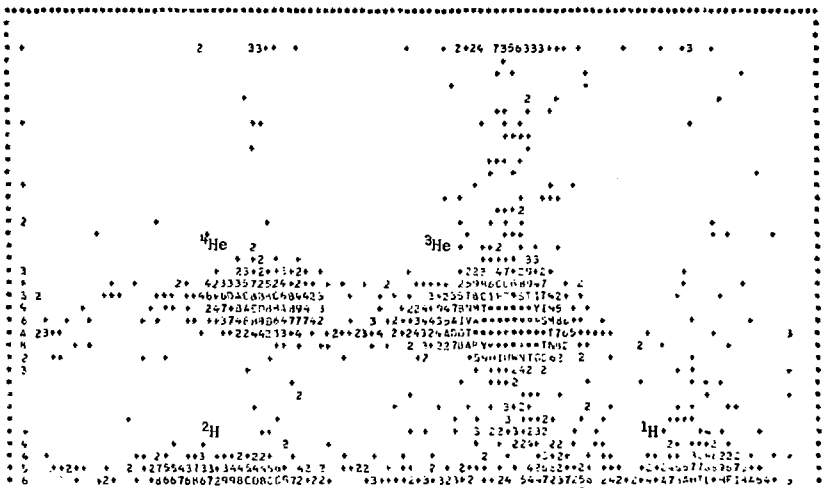

Fig. 12. Pulse height vs time-of-flight for products at rigidity p/Z = 1.25 GeV/c and θ = 0° from 1.75 GeV/c/N alphas incident on a carbon target. Protons, deuterons, ^{3}He, and alpha particles are clearly present.

XBL 779-2454

so that we could constantly determine which isotopes were present and monitor the performance of the system.

F. Electronics

For each event, the time-of-flight, the pulse heights, and the pattern of counters which fired their discriminators were read into the PDP-11/20 computer using suitable CAMAC interfaces. An event was defined by the coincidence F4·F5X·F5Y, i.e. by at least one counter firing in each of the hodoscopes F4, F5X, and F5Y. The diagram of the event data electronics is shown in Fig. 13. The anode signals of the hodoscope photomultipliers were used as inputs to the discriminators, and the dynode signals were inverted and attenuated for pulse-height measurement in the ADC's. Separate 8-channel, 8-bit ADC's were used for the F4 and F5 signals with gating signals (strobes) provided with the timing determined by the F4 and F5 signals, respectively, so that the strobes could be made as narrow as possible, thus reducing the effects of other particles nearby in time. Separate 12-channel input registers were similarly provided to record the pattern of hodoscope discriminators which fired. The time-of-flight was registered by a a 10-bit time-to-digital converter (TDC) with 0.2 ns resolution. The START signal was obtained from the OR of the F5X hodoscope, and the STOP signal from the OR of the F4 hodoscope, suitably delayed. Use of the START INHIBIT input of the TDC allowed us to inhibit any start in the TDC except when we had a trigger. Opposing pairs of phototubes viewing the PH scintillator were added together and read by ADC's. Visual and computer-read scalers were used to record the number of events, the counts in the hodoscopes, and beam monitor counters.

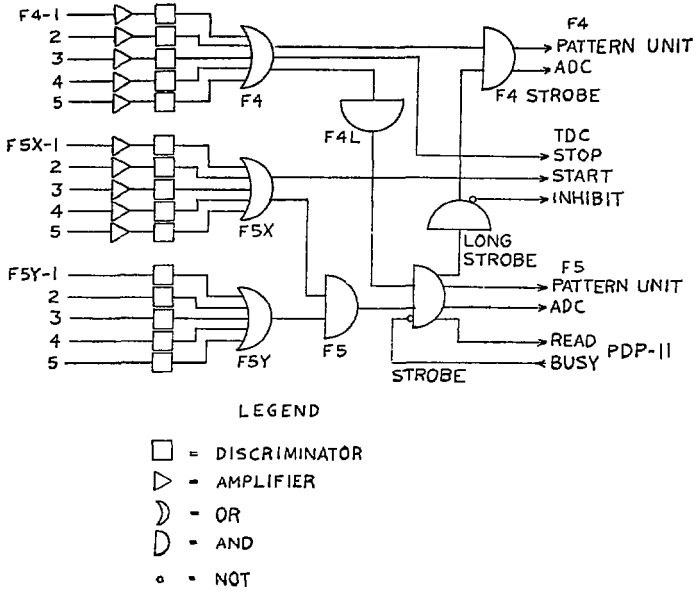

Fig. 13. Electronics of the event trigger circuit.

XBL 779-2446

The trigger strobe AND unit was gated by the computer; that is, when a strobe was generated, the unit was turned off via its VETO input and not enabled again until the computer was finished reading out the event. This gating signal was also applied to an additional set of scalers used to count the events and beam monitor counts, so that we always had an accurate measure of the dead time created by the computer.

G. Running Plan

The running procedure began with the acceleration of the primary beam particles in the Bevatron and their delivery to our target. The centering of the beam in the beam pipes was aided and monitored by multiwire proportional chambers. Then the intensity was lowered to approximately 10^4 particles/pulse and the spectrometer was set to transport the primary beam rigidity at 0°. The correctness of the magnet settings was verified by observing well focused beam spots with multiwire proportional chambers.

The actual data taking consisted of many runs of duration from one to 10 minutes designed to map out the kinematic region which the spectrometer could cover. Typically we started out at the beam rigidity at a small angle and cycled through the targets. Then we moved out in angle until we reached the limit of the spectrometer, changed rigidity and again covered the angular range, this time moving in toward 0°. Fig. 14 shows the pattern of data points taken for the 1.75 GeV/c/N α beam and how they cover the kinematic region available to us.

Typically we ran for 50,000 triggers from the C target and 10,000 from the Cu, Pb, CH_2 targets and ran with the empty target for 1/3 as

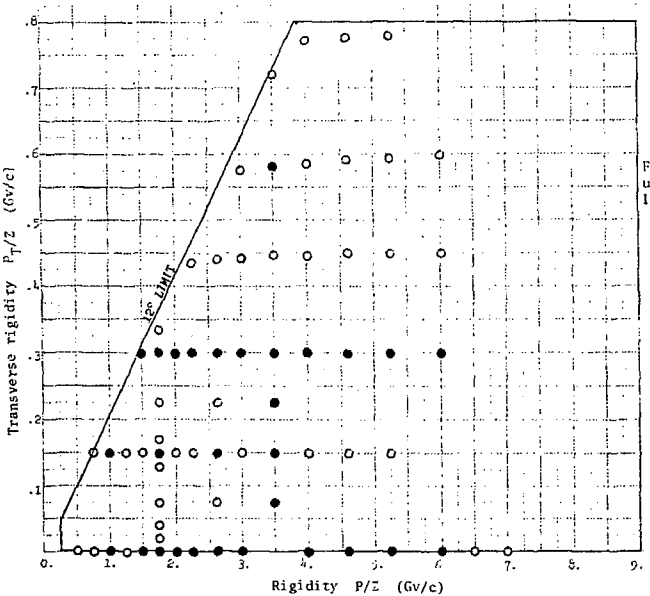

Fig. 14. Spectrometer settings used in data-taking with the 1.75 GeV/c/N alpha beam.

○ C target

● C, CH_2, Cu, Pb targets

long a time as the C target. We had the incident beam intensity adjusted to give approximately 1000 events per Bevatron pulse. We recorded approximately 13 million events in nearly 1200 runs to obtain the data covered in this work.

IV. DATA ANALYSIS

The time-to-digital converter (TDC), analogue-to-digital converters (ADC's), and the pattern of counters that fired for each event were recorded on magnetic tape. In addition, the pulse-by-pulse total counts from the counters, coincidence units, and beam monitors were recorded at the end of each beam burst. A sequence of offline computer programs was set up to identify the detected particles, to determine the amount of incident beam, to store this information, and to calculate and store the single particle inclusive cross sections.

A. Particle Identification

Particles were identified through a combination of dE/dx (specific energy loss by pulse height), time-of-flight (TOF), and magnetic rigidity measurements. To state it most simply, the charge is determined by dE/dx, the charge/mass ratio is determined by the combination of TOF and magnetic rigidity, thus yielding the mass. In practice, we used the masses and charges of the known particles which we might possibly observe and the properties of the detection system to predict their most probable TOF and ADC (pulse height) values, and then counted the number of events with values close to those predicted.

First it was necessary to sharpen up the TDC (TOF) distributions by making corrections based on the pulse heights in the F4 and F5X hodoscopes. As shown in Fig. 15, a large photomultiplier pulse will trigger a fixed-level discriminator earlier with respect to the particle passage (indicated by the peak amplitude of the pulse) than a small pulse. We corrected the TDC value of each event for this effect, called slewing,

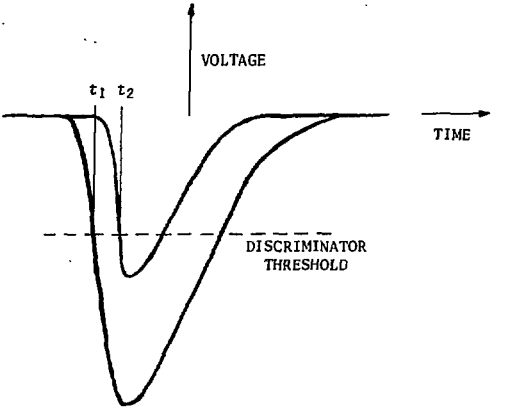

Fig. 15. Slewing; the effect of pulse height on timing measurements.

XBL 779-2466

using the F4 and F5X hodoscope ADC's and fitting the data for each hodoscope to the form $t = a_i + b_i/ADC_i$. This correction was applied to each event yielding a sharper TOF distribution, as may be seen in Fig. 16.

For each event, five measurements of dE/dx were recorded (F4, F5X, F5Y, and two from the 1/2" thick PH scintillator). Using four independent dE/dx measurements, we made an estimator of how well each event agreed with the hypothesis of each possible particle type. First, using data which was purely one particle type, we generated the ADC distribution for each counter and calculated the peak position X and mean square width W^2. This was done for a particle with charge $z = 1$ and for one with $z = 2$. To predict the peak position for particles of other velocities, we used a formula for the most probable value of energy loss[42]

$$\Delta E = \frac{z^2 A t}{\beta^2} (\ln B\gamma^2 t - \beta^2)$$

where A and B are constants dependent on the medium, t is the thickness, z and $\beta = v/c$ are the charge and velocity of the particle, and $\gamma = (1-\beta^2)^{-1/2}$. The width W was assumed to be independent of velocity.

Each event was compared against this dE/dx prediction for each possible particle type by calculating the estimator

$$X_j'^2 = \sum_i \frac{(ADC_i - X_{ij})^2}{W_{ij}^2}$$

where j refers to the particle hypothesis, i the counter, ADC_i its ADC value for this event, X_{ij} the predicted position of the ADC peak, W_{ij}^2 the mean

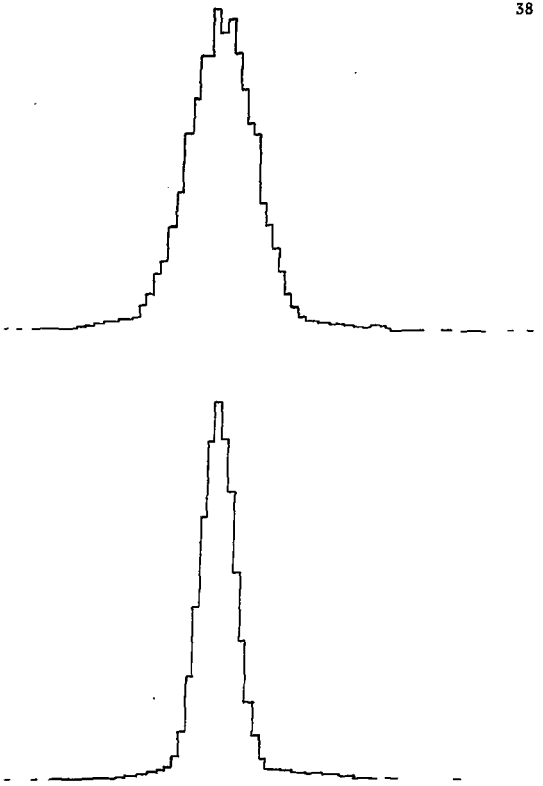

Fig. 16a. Distributions of raw TDC (above) and slewing corrected TOF (below) for Z = 1 particles; 2.88 GeV/c/N α + C → d + X, at momentum 5.76 GeV/c and angle 3°.

XBL 779-2448

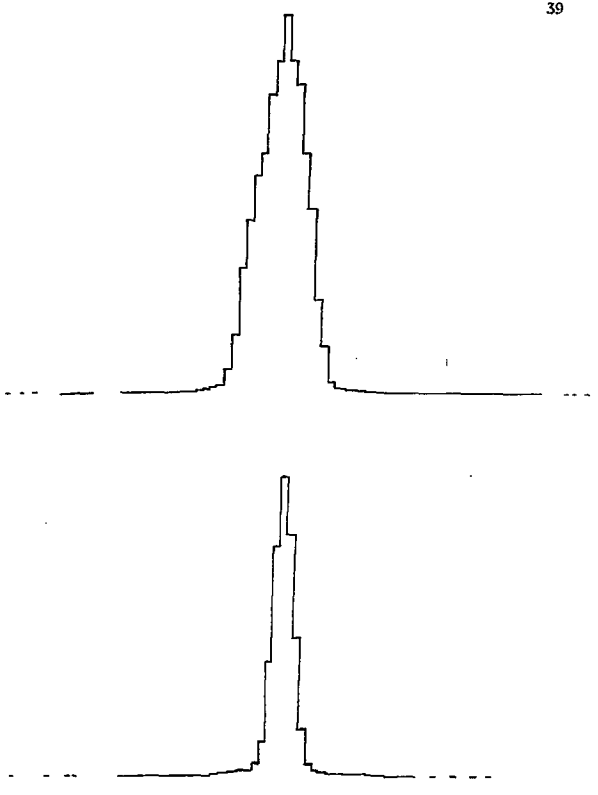

Fig. 16b. Distributions of raw TDC (above) and slewing corrected TOF (below) for Z = 2 particles; 2.88 GeV/c/N $\alpha + C \rightarrow \alpha + X$, at momentum 11.54 GeV/c and angle 3°.

XBL 779-2449

square width for the "pure" particle ADC distribution of counter i and of the same charge as particle type j. The sum extends over up to 3 of the 4 counters: we omit the one which would give the largest contribution to the χ'^2 and any that overflow. Although the method of calculation of χ'^2 is the same as that for the traditional χ^2, the distribution of dE/dx is not Gaussian--in fact there is a very long high-dE/dx tail--so that it is not a true χ^2. The distributions of χ'^2 for the deuteron and alpha hypotheses obtained at rigidity $P/z = 5.76$ GV/c and $\theta = 3°$ are shown in Fig. 17. The requirement $\chi'^2 \leq 3$ is satisfied by 97.5-99% of the particles of correct charge and less than 0.05% of the particles of wrong charge.

Two methods were used for determining the number of identified particles of each type from the χ'^2 and TOF. In the first method, used at low momenta where the particles are well separated in TOF, we had the χ'^2 and TOF distributions printed out for each rigidity setting. From these distributions we determined cuts which would unambiguously identify each particle.

In the second method, used at higher momenta where the TOF distributions of different particles were overlapping, we constructed for each particle hypothesis the TOF distribution of events having $\chi'^2 \leq 3$ and compared this with a model TOF distribution for particles of that charge similarly obtained from a sample of data in which only one particle type was present. We used, typically, the ^3H peak for $z = 1$ and the alpha beam for $z = 2$.

The model TOF distribution was used to determine the tail of each particle type's TOF distribution under the peak of the other in the

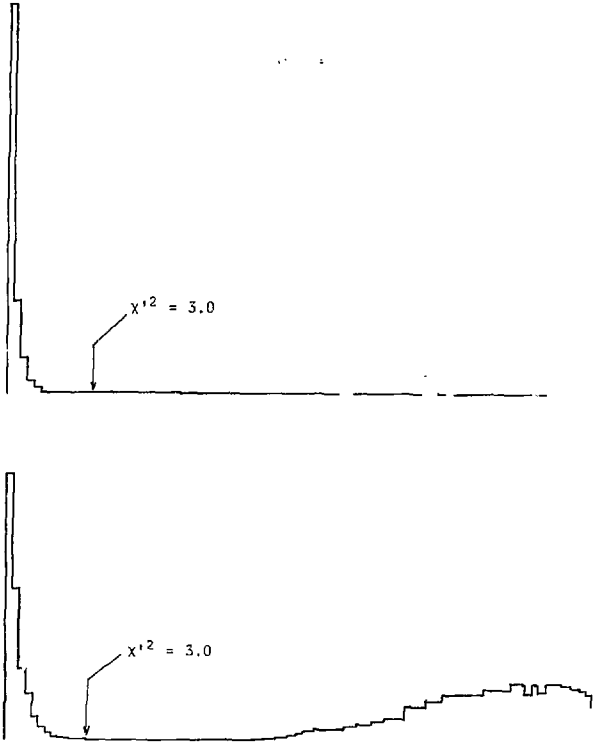

Fig. 17. Distribution of χ'^2 for deuteron (above) and alpha (below) hypotheses at magnetic rigidity P/Z = 5.76 GV/c and angle 3° for 2.88 GeV/c/N alphas on a carbon target.

XBL 779-2450

following way: Let $M_c(t)$ be the number of particles in the model TOF distribution falling within a certain size cut centered at distance t channels from the peak of the distribution, and let M be the total number of particles in the distribution. Then define the function $F(t) = M_c(t)/M$. Now consider the TOF distribution for a run of data in which we have two neighboring peaks of particles A and B in the TOF distribution as shown in Fig. 18. Let A_c and B_c be the number of particles within the cuts placed about the predicted peak positions for particles A and B, respectively, and let A_T and B_T be the total numbers of particles A and B. Then, assuming that A and B have TOF distributions of the same shape as the model distribution,

$$A_c = A_T \cdot F(0) + B \cdot F(-t)$$

$$B_c = B_T \cdot F(0) + A \cdot F(t)$$

where t is the time distance in channels between particles A and B. This pair of equations is easily solved for A_T and B_T. The straightforward generalization of this procedure to any number of particle types was used in the analysis. This procedure was checked using "pure" particle samples and by comparing the results with those obtained by manually subtracting the backgrounds and was monitored by checking that the total number of identified particles agrees with the total number of events in a run. The χ'^2 and TOF distributions were also printed for each rigidity and checked against predictions. The agreement of the empirical TOF distributions with that of the model was monitored by performing the identification using 3 different cut widths and checking their agreement. The largest cut width was used for the cross section calculations.

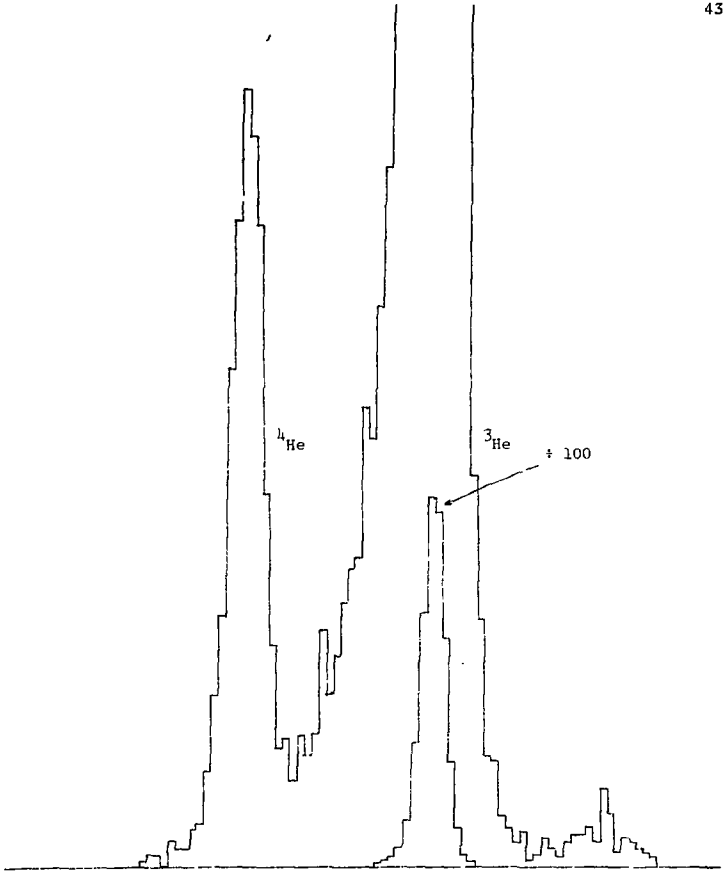

Fig. 18. Distribution of TOF for Z = 2 particles at momentum 5.25 GeV/c and angle 0° from 1.75 GeV/c/N alphas incident on a carbon target.

XBL 779-2451

In a few cases we found it necessary to make a slight modification of this second method. For example, at momenta above that of the ^3H peak we observed events with a TOF the same as that for ^3H at the peak velocity, as shown in Fig. 19. No known particle at the rigidity the spectrometer was set to select could have such a velocity. This contamination is apparently the result of the much more populous peak particles scattering in the spectrometer in such a way as to mimic the momentum selection (the ^3H cross section falls by a factor 5×10^{-3} between 5.25 and 6.0 GeV/c in the example shown in Fig. 19). To avoid counting these contaminating particles, we moved the TOF cuts so they included only the central channel and the side of the distribution away from the contamination.

To the particle totals thus obtained we have made the following necessary corrections:

1) In order to reduce the contamination of the z = 1 TOF distribution from z = 2 particles which fragment in the system (seen in Fig. 12 as particles having ^3He TOF but z = 1 dE/dx), we consider for the z = 1 χ'^2 hypotheses only those events which have at F4 an ADC less than the minimum seen for z = 2 particles at that velocity. Thus we must correct for the tail of the z = 1 dE/dx distribution beyond this cut. This is typically 0.4%.
2) The correction for the cut on χ'^2 was typically 1 to 2.5% and was determined from "pure" particle data samples.
3) Approximately 0.02% of the deuterons are misidentified as alphas because they have large pulse heights in several counters, and thus we must subtract this fraction of the deuterons from the

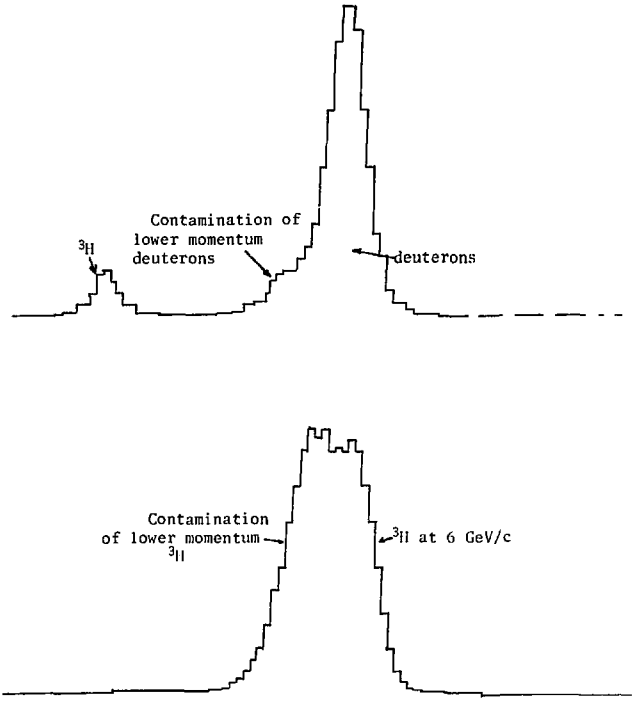

Fig. 19. TOF distributions showing contamination of data with events from a different momentum.
(Above) 1.75 GeV/c/N α + C → d, ^{3}H + X at momentum 4 GeV/c and angle 0°.
(Below) 1.75 GeV/c/N α + C → ^{3}H + X at momentum 6 GeV/c and angle 0°.

XBL 779-2452

alpha total. The amount of this correction is determined by asking the program to identify ^{6}He for data at the ^{3}H peak.

B. Calculation and Normalization of Cross Sections

The single particle inclusive cross section in the laboratory Lorentz frame is given by the formula

$$\frac{d^2\sigma}{d\Omega dp} = \frac{N_t}{B_t}\frac{1}{\eta}\frac{1}{d\Omega dp/p}\frac{1}{p_0} \qquad (1)$$

where N_t is the number of identified particles of a given type produced in the target, B_t is the number of beam particles incident on the target, η is the number of target nuclei per unit area listed in Table 1, $d\Omega dp/p$ is the solid angle-momentum acceptance of the detectors, and p_0 is the central momentum of the detected particles (particle charge × rigidity setting).

Since the other quantities have already been specified, we consider now the calculation of N_t/B_t. If we use the ion chamber (IC) or secondary emission monitor (SEM) as our beam monitor then, ignoring the fact that a small amount of the beam that is counted by the ion chamber misses the target, we have B_t = V C K where V is the voltage the IC or SEM produced across capacitance C, and K is the number of incident alpha particles per unit charge, i.e. the IC or SEM calibration constant.

Since the events read in by the computer are gated by the computer-generated dead time, and the IC and SEM are not, we need to make a correction for this dead time, using the numbers of gated events G and ungated

events U. If this correction is applied to the beam monitor, then the number of events per beam particle is N/B = NU/(GVCK). Finally, we must use the empty target run to subtract off production from sources other than the target. This gives

$$\frac{N_t}{B_t} = \left[\left(\frac{NU}{GVC}\right)_F - \left(\frac{NU}{GVC}\right)_{MT}\right] \frac{1}{K}$$

where subscripts F and MT refer to the full and empty target runs, respectively. Here N is the number of identified particles of a given type, some of which may come from sources other than the target. B is the number of beam particles when corrected for deadtime, of which B_t hit the target.

If we use one of the monitor telescopes M1, M2, or M3 as our primary beam monitor, we can take into account the fact that not all the beam may be intercepted by the target. In this case $N_t/B_t = N_t(M_t K_i)$, where M_t is the number of counts in monitor telescope M1, M2, or M3 from particles produced in the target and K_i is the calibration factor for that monitor discussed in Appendix II. For full and empty target runs of equal length $N_t = N_F - N_{MT}$. Since the runs were not of equal length we must weigh the empty target run by the incident beam. For this purpose we use the ion chamber and the live-time factor G/U, obtaining

$$N_t = N_R - N_{MT}\left(\frac{VCG}{U}\right)_F \Big/ \left(\frac{VCG}{U}\right)_{MT} .$$

We obtain M_t in a similar manner, correcting the ion chamber with the ratio M/m where m is the number of ungated monitor counts. The result is

$$\frac{N_t}{B_t} = \frac{N_F - \left(\frac{NU}{VCG}\right)_{MT}\left(\frac{VCG}{U}\right)_F}{KM_F\left[1 - \left(\frac{m}{VC}\right)_{MT}\left(\frac{VC}{m}\right)_F\right]} .$$

Cross sections were calculated by these procedures for all the beam monitors, and the results were compared in order to determine the range in primary beam intensity and production angle over which the various monitors were reliable. Telescope monitor M3 was used for the majority of the final cross section calculations and M1 was used occasionally at low intensities, since it is more sensitive. For one segment (the majority) of the 2.88 GeV/c/N data, unstable behavior in the telescopes forced us to use the IC as the primary beam monitor. In order to take into account the small fraction of beam missing the target, we compared the data with repeated measurements made later using M3 for normalization. The results were consistent with 1.7% of the beam missing the target on the average. This correction was applied to the normalization.

The 5 × 5 × 5 array of hodoscopes F4, F5X, and F5Y allowed us to make finer determination of the momentum and angular dependence of the cross sections. For this purpose we calculated the cross section for each particle type at each rigidity and angle setting, using 12 different angle and momentum bins. Bins 1-5 are the angle bins averaged over momentum obtained by binning according to which one of the five F5Y counters fired. The angular resolution of each bin is approximately ±1.9 mr and the momentum resolution is ±3%. Bins 6-10 are the momentum bins, and their approximate ranges of acceptance are shown in Fig. 20. The momentum resolution resulting is ±0.6% for bins 2, 3, 4 and ±1% for bins 1 and 5. The angular resolution is ±9.5 mr. Bin 11 is the central bin consisting of events falling in the central 3 counters in F4, F5X and F5Y. It has angular resolution ±5.7 mr and momentum resolution ±1.8%. Bin 12 is the "total" bin consisting of all events. Its angular resolution is ±9.5 mr and its momentum resolution is ±3%.

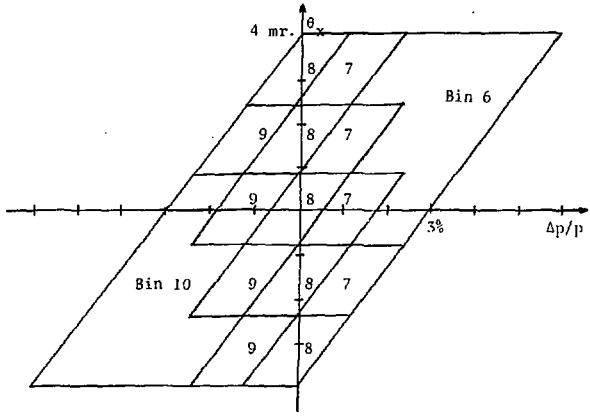

Fig. 20. Approximate areas of acceptance in momentum and horizontal angle for cross section bins 6-10 (the momentum bins) according to first order optical theory of the spectrometer.

XBL 779-2453

The full-empty target subtraction was applied separately for each bin in the manner described above, and the errors quoted for each bin include the normalization uncertainty for that run, i.e. each bin is treated as an independent data point.

C. Corrections to the Data

The data were corrected for energy loss and absorption in the target. The energy loss correction was made using the Bethe-Bloch equation[43] and the tables of Barkas and Berger.[44] The correction ranged from 0.1% for fast protons up to 8.3% for 1.5 GeV/c ^{3}He in the lead target. The absorption corrections were made using the results of Jaros[40] and the energy dependence of the nucleon-nucleon total cross section.[45] This correction varied from 1.2% for protons in the copper target to 3.8% for alphas in the CH_2 target. The cross sections so calculated are listed in Table 4.

D. Sources of Error

For the purposes of this discussion of the errors associated with the measurement and calculation of the cross section, we may divide the possible sources of error into three types: 1) internal relative uncertainties, i.e. those errors that apply to each cross section independently and determine the uncertainty in the relative values of the cross sections within the experiment; 2) the overall normalization uncertainty; 3) errors associated with special conditions.

The errors listed in Table 4 include all known sources of error of type 1. These include the statistical uncertainties in the numbers of particles identified and in beam monitor counts, and the uncertainty in the ion chamber background (no beam) signal. The uncertainty in the measured target thicknesses (∿0.8%), the uncertainty in the calibrations of the beam monitors relative to each other (∿2%), and the uncertainty in the settings of the spectrometer magnets (typically ≤1%) are also included. The errors in the corrections made in the particle identification are the following: the model time-of-flight distribution correction (30%), the χ'^2 cut correction (40%), Landau tail cut correction for Z = 1 particles (50%) and the tail of deuteron χ'^2 distribution to be subtracted from the alphas (50%). The smallest errors resulting from the composition of these many sources of error are approximately ±6%.

Fig. 21 shows measured Lorentz invariant single particle inclusive cross section for the reaction 1.75 GeV/c/N $\alpha + C \rightarrow p + X$ for protons at a momentum of 1.75 GeV/c and with transverse momentum in the neighborhood of 0.15 GeV/c.

Cross sections were measured using all four of the carbon targets: the standard 1/2" thick and the "large," "small," and thin (1/4") carbon targets. In addition, the measurement with the standard carbon target was repeated two weeks later. Examination of these and other repeated measurements, and of the smoothness of the data, leads us to believe that the tabulated errors well represent the relative uncertainties of the cross sections. The uncertainty in the overall normalization comes from two sources: the calibration of the ion chamber (2%) and the calibration of the acceptance of the spectrometer and detectors (8%). The resulting error of ±8.1% is not included in the errors quoted in Table 4.

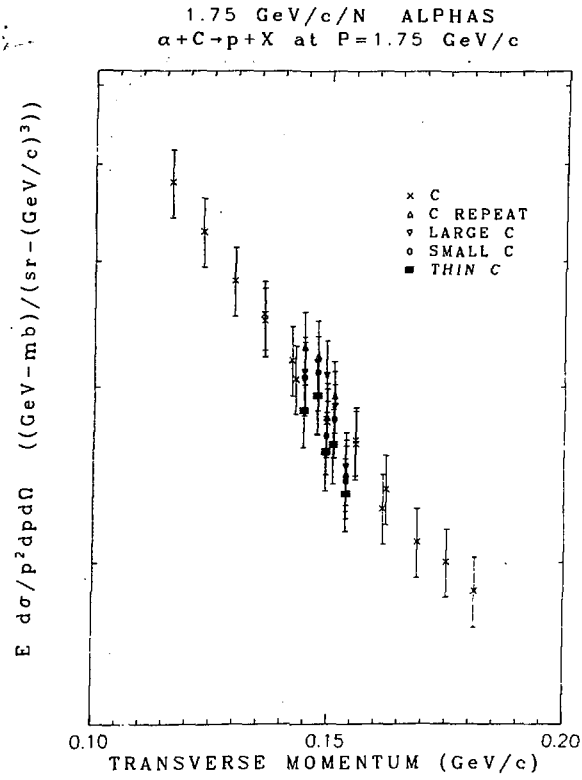

XBL 777-9767

Fig. 21. Repeated measurements of the Lorentz invariant single particle inclusive cross section for the reaction 1.75 GeV/c/N $\alpha + C \rightarrow p + X$ at 1.75 GeV/c and p_T near .15 GeV/c. All four carbon targets were used during one run session and the standard carbon target measurement was repeated two weeks later.

Other errors which apply in different situations to a greater or lesser degree were not included in the tabulated errors. Since the cross section often changes very rapidly with angle and momentum, a small error in the angle or momentum can lead to a large error in the resulting cross section if the angle and momentum are assumed to be correct. The uncertainties in the angle and momentum are due to uncertainty in the accuracy of the hardware and software which set and control the magnet currents. Fortunately these uncertainties are greatest at low momenta where the cross section is usually relatively flat and the uncertainty is of little consequence. The error in the momentum setting is a constant 4 parts in 4096 of the maximum momentum setting for magnets M8A, M8B, M1 and M2. This gives $\Delta p = 0.0091$ GeV/c. The error in the angle setting is composed from the uncertainty in the settings of M6V and M7V

$$\Delta\Theta = 0.0014(Z/P)_{\text{BEAM}} + 0.0016(Z/P)_{\substack{\text{DETECTED} \\ \text{PARTICLE}}} .$$

Multiple coulomb scattering of the primary beam and the produced particles in the target material contributes to the measured cross sections, broadening the angular distributions. This is worst for the case of 0.93 GeV/c/N α + Pb $\rightarrow \alpha$ + X at momentum 3.72 GeV/c--the sharpest angular distribution seen in the experiment. The angle at which the angular distribution from multiple Coulomb scattering has fallen to 1/e of its peak value is $\theta_{1/e} = 11.7$ mr, so $p_{T1/e} = 43$ MeV/c, a width which is comparable to that of the observed angular distribution at small p_T (see Fig. 37), thus masking the part of the distribution due to the nuclear force. The effect of multiple Coulomb scattering is much less

for most other situations, and the data have not been corrected for its effects.

Occasionally, in data taken at production angle $\theta=0°$, the lowest momentum bin (bin 10) had a cross section result which was inconsistent with the rest of the data. Examination of the numbers of events in the momentum bins for the full and empty target runs revealed that a disproportionately large number of events often occurred in bin 10 in both full and empty target runs, at $\theta = 0°$. When bin 10 was inconsistent it was also observed that the ratio of event rates in the empty and full target runs for this bin was very inconsistent with the other 5 bins, often exceeding a value of 0.6. This effect was attributed to particles produced by collision of the beam with material upstream of our target, since there are no bending magnets between the first focus after the exit of the Bevatron and our target. A slight shift in the circulating intensity or radius, extraction radius, or external tuning could cause collisions with the beam pipes. The bulk of this production from upstream of our target was seen to occur in bin 10. If the shift occurred during a full-empty target sequence, then the result of the subtraction for this bin would not reflect the true cross section for the target material. For this reason, data points for bin 10 which were inconsistent with neighboring points by more than 1.5 standard deviations and for which the empty/full target event rate ratio was 50% different from that of the other bins were removed from the data sample.

Another effect which could produce incorrect cross sections at low momentum settings is the uncertainty in the magnet settings. If the settings of the different magnets are not matched, i.e. do not transmit

the same momentum down the center of the channel, then the acceptance of the spectrometer may be lower than at higher momenta where the relative uncertainties in the settings is less. This could result in the measured cross section's being 5% low at $p_0 = 0.5$ GeV/c.

E. Editing of the Data

Not all of the cross sections calculated by the methods described in Sections A and B are included in Table 4. Because of the very large quantity of data, we felt it necessary to produce a sample which was trustworthy and which exhibited all the essential features of the data. In order to accomplish this the data were edited according to a set of flexible but not arbitrary criteria.

First, we eliminated all cross sections of bin 12 with relative errors greater than 75% and all cross sections of bins 1-11 with relative errors greater than 50%, since the number of events for such errors is so small that they may be tails of distributions of other particle types.

In addition, other cross sections were eliminated when it was clear that there was this type of contamination even though the errors calculated were less than 50%. The high momentum tail of the deuteron distributions at small production angles was actually seen to level off. This was clearly due to contamination by the much more populous tritons and indicates that the model time-of-flight distribution is less accurate at velocities away from the beam velocity. Also for the reaction 2.88 GeV/c $\alpha + C \rightarrow {}^3H + X$ at $\theta = 0°$ we see a peak in the momentum distribution of ^3H at $p = 2.88$ GeV/c, i.e. right under the proton peak. In the same momentum

region the ^{3}He distribution is falling with momentum and charge independence is violated by more than a factor of 3 in the calculated cross sections. In other momentum regions charge independence holds to approximately 10%, a result consistent with other reactions involving ^{3}H and ^{3}He.[46]

Finally, as described in Section D, bin 10 cross sections were omitted at production angle $\theta = 0^\circ$ when both the cross section and the ratio of event rates for the empty and full targets were inconsistent with nearby points.

Table 4.

(See inside back cover.)

V. RESULTS AND CONCLUSIONS

The results are listed in Table 4, organized according to the momentum per nucleon of the projectile alpha, the target material, the momentum and angle setting of the spectrometer, the type of detected particle and the 12 angle and momentum bins within a given setting of the spectrometer. The Lorentz invariant single particle inclusive cross sections and their associated errors--including all sources of error except the overall normalization uncertainty of ±8% for the experiment--are listed in units of mb-GeV/(sr-(GeV/c)^3). Momenta are in GeV/c and angles in degrees.

The invariant cross section is plotted in Figs. 24-71 with the error bars on the ordinate taken from Table 4 and the error bars for the abscissa (indicating the bin width) only plotted when the bin being plotted is bin 12--the whole spectrometer bin. The data plotted have been edited further to keep the number of points on a plot at the minimum necessary to demonstrate the dependence of the cross section on the abscissa. Thus we use bins 1-5 for plotting vs transverse momentum and bins 6-10 for plotting vs longitudinal variables. Bin 12 is used when the finer bins have been edited out according to the criteria in Section IV E, or when the cross section is relatively constant and the finer bins would add no information to the graph.

In some instances, the apparent dependence of the plotted cross section on the abscissa is not smooth. There are two types of situations in which this occurs:

1) The transverse momentum distributions at non-zero production angle,

where the cross section falls steeply with momentum, appear to be discontinuous with an apparently high cross section in the high angle bins for each spectrometer setting. An example of this is the transverse momentum distribution of deuterons from 2.88 GeV/c/N $\alpha + C \rightarrow d + X$ at p = 6.75 GeV/c, shown in Fig. 42. The momentum distribution at 6.75 GeV/c is very steep as may be seen in Fig. 29. When we take into account the second order effects in the spectrometer optics (chromatic aberrations) the vertical acceptance is smaller (i.e. the magnification from focus F3 to F5 is smaller) for momenta below the central momentum of the spectrometer and higher for higher momenta. As a result the angle bins are closer together in angle at a given setting for the low momentum particles and farther apart for the high momentum particles. Since nearly all the events in above mentioned examples are in the low momentum end of the acceptance, the angle bins are really measuring more closely spaced angles for those events than the nominal values. Of course the central bins (bins 3, 11, 12) do give a correct and smooth distribution.

2) The momentum distribution at high momenta and non-zero angles shows an apparently lower cross section in the higher momentum bins within a given spectrometer setting. For example the deuterons from the reaction 2.88 GeV/c/N $\alpha + C \rightarrow d + X$ in Fig. 29 show this effect. This results from the fact that we are not really plotting at constant p_T = .58 GeV/c, since the higher momentum bins sample a higher transverse momentum (though partially reduced by angle-momentum correlation introduced by vertical bending magnet M7V) and thus see a lower cross section.

Except in Figs. 64-71, where the curves are computer-drawn fits, all curves are hand drawn to guide, but, we hope, not unduly prejudice, the eye of the reader.

A. General Characteristics

Fig. 24 shows the 0° spectrum of fragments from the collision of 0.93 GeV/c/N alphas with a carbon target. Namely, we have plotted the invariant cross section for the production of protons, deuterons, ^{3}H and ^{3}He at angle 0° versus the momentum of the produced fragment. Figs. 25 and 26 show similar spectra for the 1.75 and 2.88 GeV/c/N alpha beams, respectively. The major features evident are: 1) Projectile fragmentation peaks for each fragment at the same momentum per nucleon as the projectile, 2) a central plateau or valley at intermediate momenta, 3) the tail of the target fragmentation distribution at low momenta. In comparing Figs. 24, 25, and 26 with each other we see that the heights of the peaks are independent of projectile energy, whereas the cross section in the central region decreases with projectile energy, especially for the heavier fragments. In fact in this central region the cross sections for ^{3}H and ^{3}He fall by a factor of 100 between 0.93 and 2.88 GeV/c/N. Fig. 27 shows the same data as Fig. 26 plotted against rapidity. The persistence of velocity and the clear separation between the projectile and fragmentation regions are evident.

The near equality of the ^{3}H and ^{3}He cross sections is apparent in Figs. 24-26, with the ^{3}H cross section being approximately 10% higher. This result is in approximate agreement with isospin invariance of the nuclear force, with the 10% deviation from exact equality of the cross sections being the same as the deviation observed in the exclusive reactions $p + d \rightarrow {}^3H + \pi^+$, $^3He + \pi^0$, as predicted from electromagnetic effects.[46]

Fig. 28 shows the momentum distribution of protons at several values of transverse momentum for 2.88 GeV/c/N alphas incident on carbon. Figs.

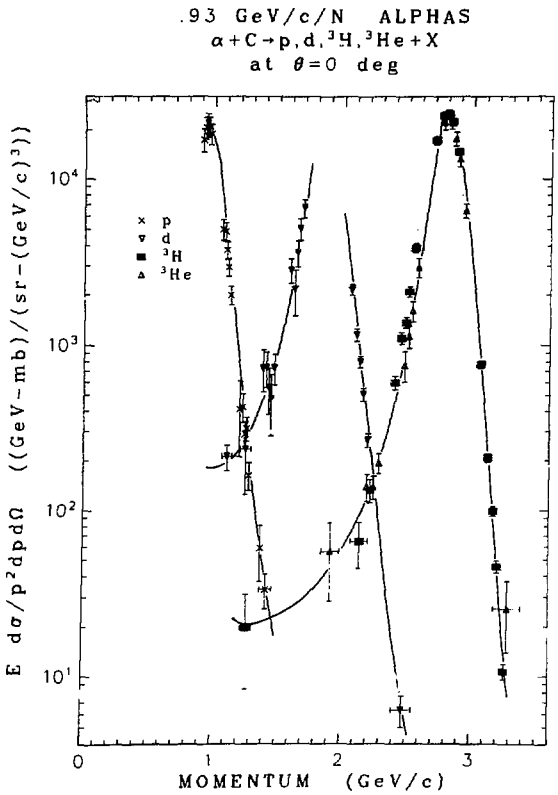

XBL 778-9785

Fig. 24

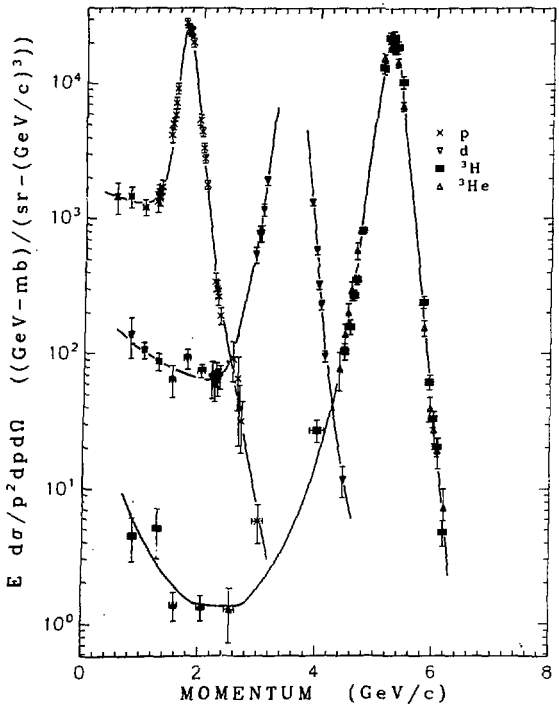
1.75 GeV/c/N ALPHAS
α+C→p,d,³H,³He+X
at θ=0 deg
E dσ/p²dpdΩ ((GeV-mb)/(sr-(GeV/c)³))
MOMENTUM (GeV/c)
p
d
³H
³He
XBL 778-9788

Fig. 25

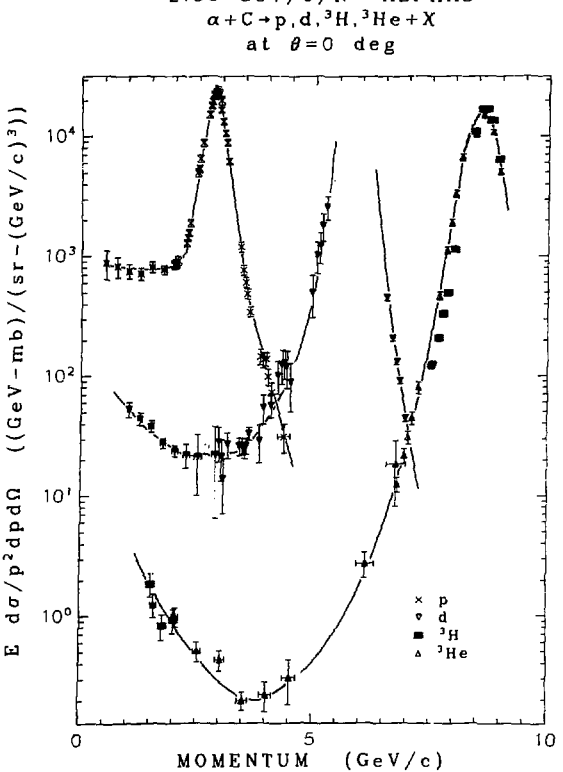
2.88 GeV/c/N ALPHAS
α+C→p,d,³H,³He+X
at θ=0 deg
E dσ/p²dpdΩ ((GeV-mb)/(sr-(GeV/c)³))
10⁴
10³
10²
10¹
10⁰
0
5
10
MOMENTUM (GeV/c)
p
d
³H
³He
XBL 778-9778

Fig. 26

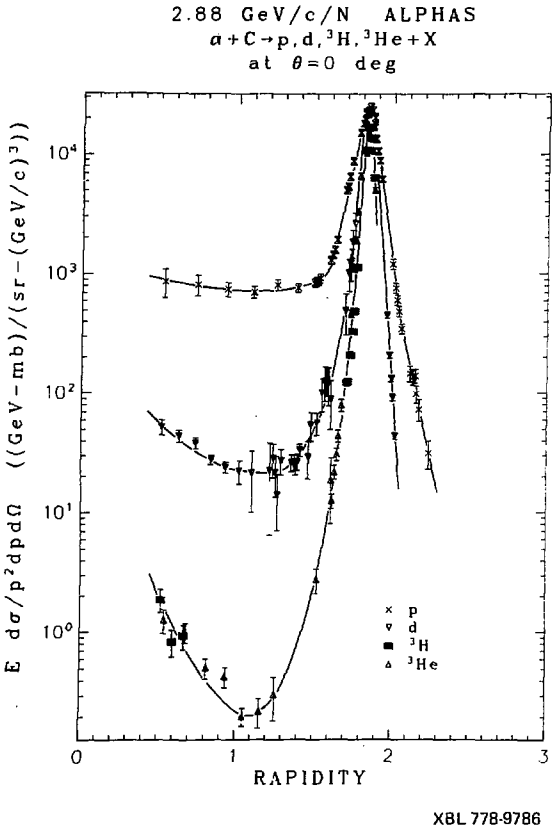
2.88 GeV/c/N ALPHAS
a+C→p,d,³H,³He+X
at θ=0 deg
E dσ/p²dpdΩ ((GeV-mb)/(sr-(GeV/c)³))
RAPIDITY
p
d
³H
³He
XBL 778-9786

Fig. 27

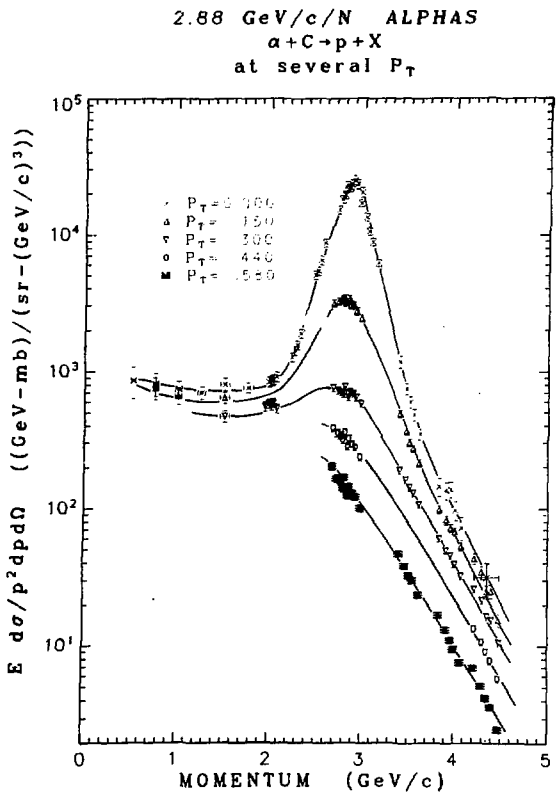
2.88 GeV/c/N ALPHAS
α+C→p+X
at several P_T
P_T = 0.100
P_T = 1.50
P_T = 3.00
P_T = 4.40
P_T = 5.80
E dσ/p²dpdΩ ((GeV-mb)/(sr-(GeV/c)³))
MOMENTUM (GeV/c)
XBL 778-9780

Fig. 28

29-31 show the analogous distributions for d, ^{3}H (from 1.75 GeV/c/N alphaa), and ^{3}He, respectively. The fragmentation peaks are seen to be sharply peaked in transverse momentum, so that, for instance, in Fig. 28 at p_T = 0.44 GeV/c there is only a shoulder at p = 2.88 GeV/c, rather than the sharp peak seen in the p_T = 0 spectrum. At momenta beyond the fragmentation peak, an approximately exponential decrease of the cross section with momentum is evident, with a slope which is nearly independent of transverse momentum. In addition, the momentum at which the cross section peaks at a given p_T shifts to lower values at larger p_T. This indicates the kinematic effect of scattering from the target and implies that the sudden approximation does not adequately describe the data, not even out to p_T = 0.15 GeV/c.

Fig. 32 shows the momentum spectrum of protons produced at 0° by 2.88 GeV/c/N alphas incident on each of the targets: H, C, Cu, and Pb. The cross section is only weakly target dependent beyond p = 2.5 GeV/c but is increasingly target dependent at lower momenta, so that, for the heavier targets, the tail of the target fragmentation region extends quite close to the projectile fragmentation region. This target dependence is stronger yet at low momenta for the heavier fragments; the d, ^{3}H, and ^{3}He distributions may be seen in Figs. 33-35, respectively. Fig. 36 shows the 0° production of protons from 2.88 GeV/c/N alphas incident on the four targets, i.e. the same data as Fig. 32, plotted against the proton rapidity. This shows more clearly that we see only the tail of the target fragmentation region.

We now examine some transverse momentum distributions. Fig. 37 shows the p_T distribution of alpha particles scattered at the beam momentum from 0.93 GeV/c/N alphas incident on the four targets. Figs. 38 and 39 show the analogous results for the 1.75 and 2.88 GeV/c/N alpha beams, and Fig.

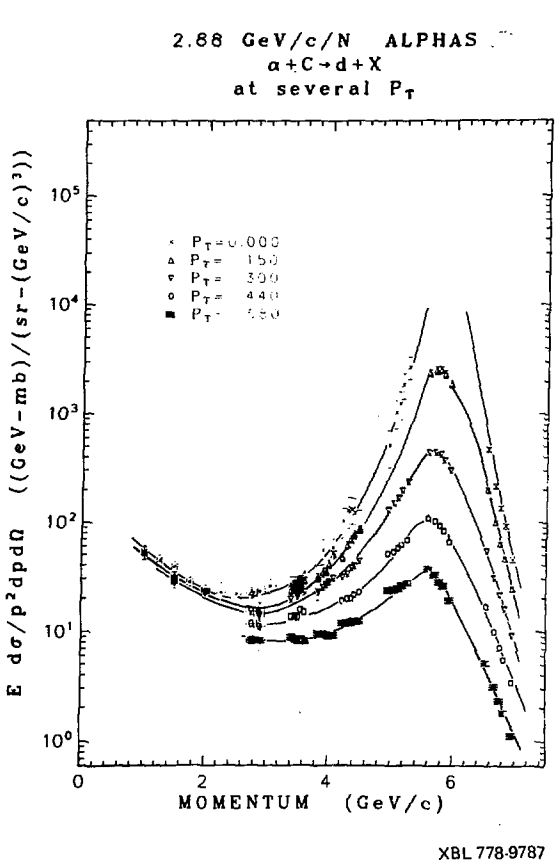
2.88 GeV/c/N ALPHAS
α+C→d+X
at several P_T
P_T=0.000
P_T= 150
P_T= 300
P_T= 440
P_T= 520
E dσ/p²dpdΩ ((GeV-mb)/(sr-(GeV/c)³))
MOMENTUM (GeV/c)
XBL 778-9787

Fig. 29

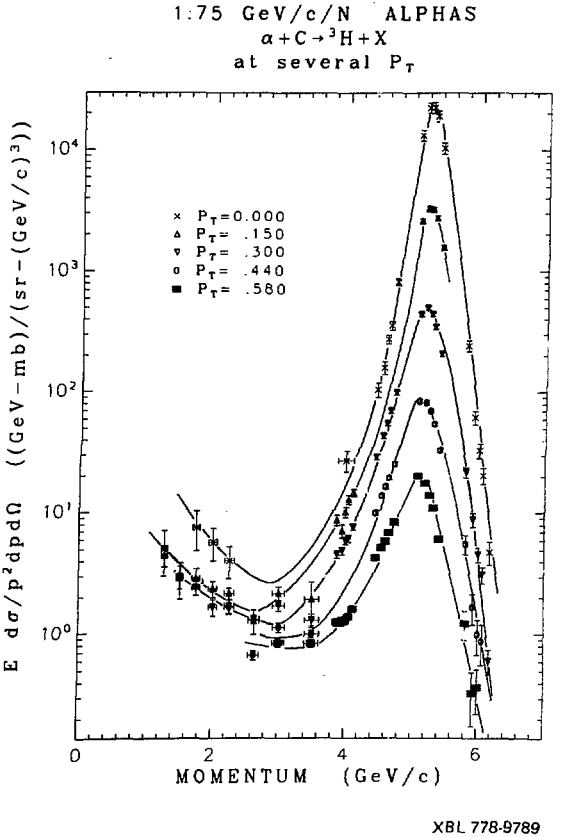
1.75 GeV/c/N ALPHAS
α+C→³H+X
at several P_T
E dσ/p²dpdΩ ((GeV-mb)/(sr-(GeV/c)³))
MOMENTUM (GeV/c)
P_T=0.000
P_T= .150
P_T= .300
P_T= .440
P_T= .580
XBL 778-9789

Fig. 30

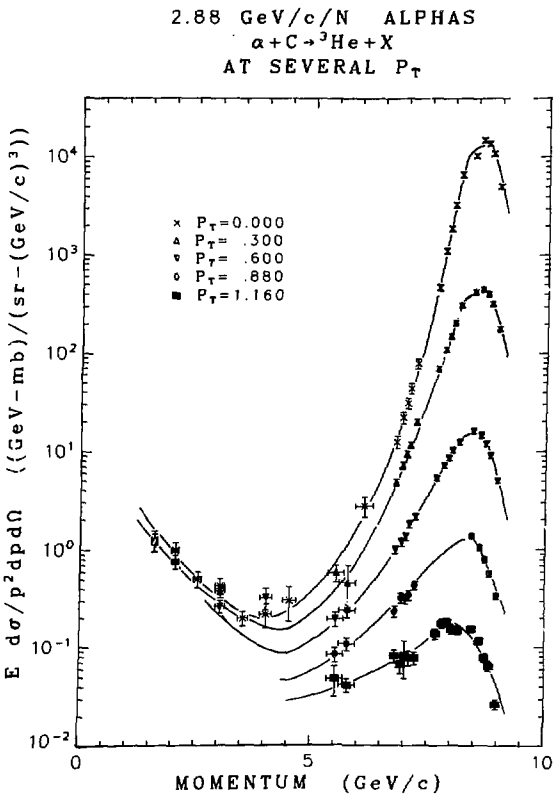
2.88 GeV/c/N ALPHAS
α+C→³He+X
AT SEVERAL P_T
× P_T=0.000
△ P_T= .300
▽ P_T= .600
○ P_T= .880
■ P_T=1.160
E dσ/p²dpdΩ ((GeV-mb)/(sr-(GeV/c)³))
10⁴
10³
10²
10¹
10⁰
10⁻¹
10⁻²
0
5
10
MOMENTUM (GeV/c)
XBL 7/8-2617

Fig. 31

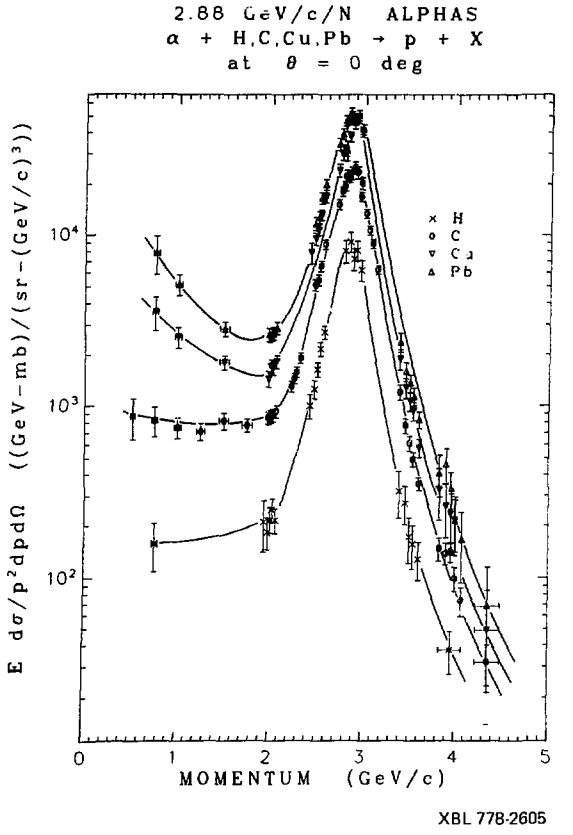
2.88 GeV/c/N ALPHAS
α + H,C,Cu,Pb → p + X
at θ = 0 deg
E dσ/p²dpdΩ ((GeV-mb)/(sr-(GeV/c)³))
10⁴
10³
10²
× H
o C
▽ Cu
△ Pb
0
1
2
3
4
5
MOMENTUM (GeV/c)
XBL 778-2605

Fig. 32

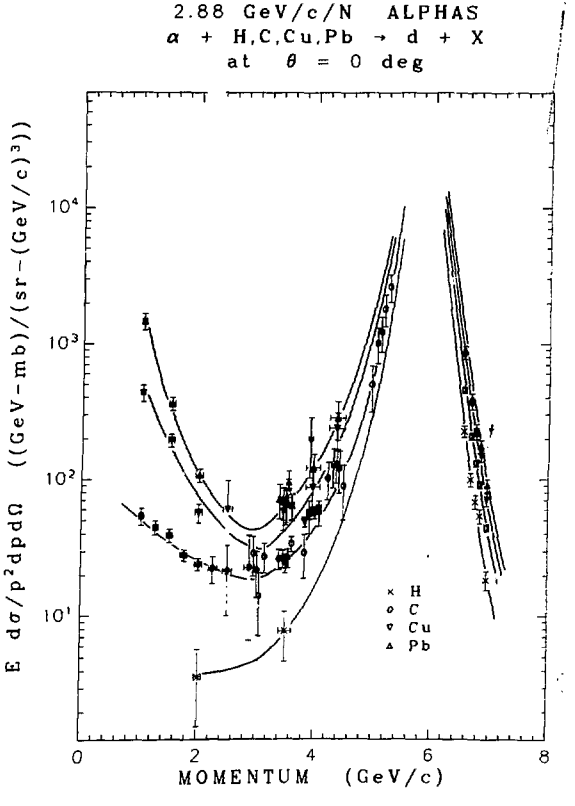

XBL 778-2607

Fig. 33

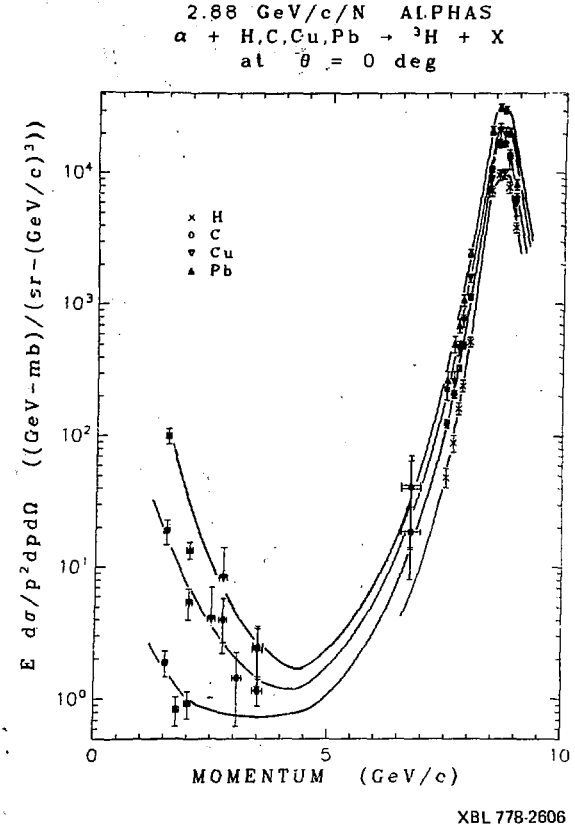
2.88 GeV/c/N ALPHAS
α + H,C,Cu,Pb → ³H + X
at θ = 0 deg
E dσ/p²dpdΩ ((GeV-mb)/(sr-(GeV/c)³))
10⁴
10³
10²
10¹
10⁰
× H
o C
▽ Cu
▲ Pb
0
5
10
MOMENTUM (GeV/c)
XBL 778-2606

Fig. 34

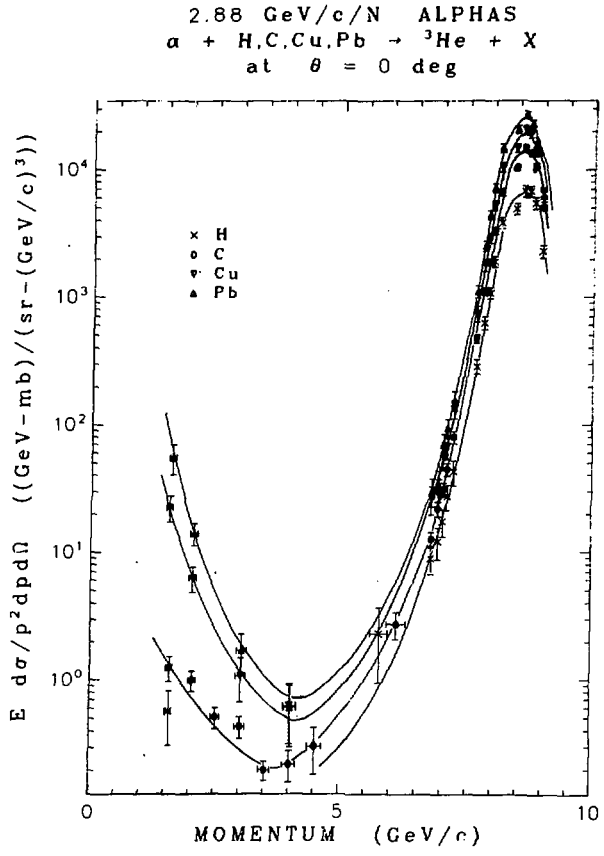

XBL 778-2608

Fig. 35

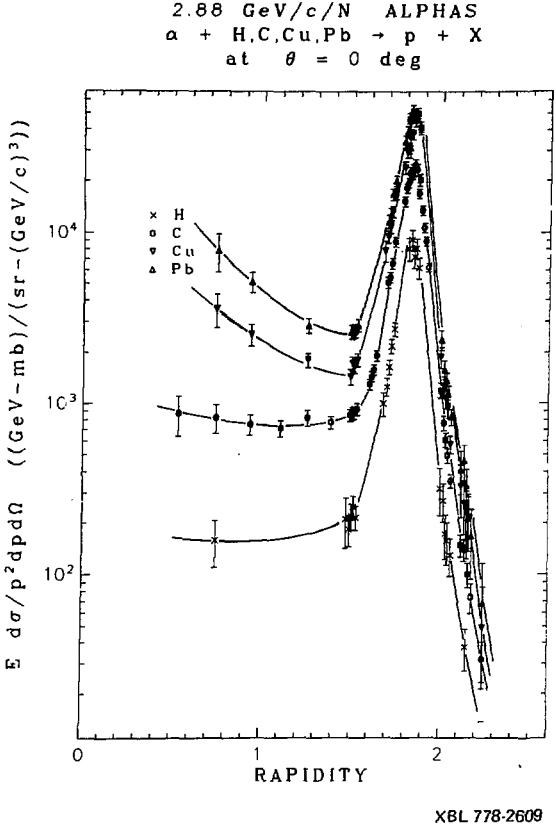
2.88 GeV/c/N ALPHAS
α + H,C,Cu,Pb → p + X
at θ = 0 deg
H
C
Cu
Pb
E dσ/p²dpdΩ ((GeV-mb)/(sr-(GeV/c)³))
10⁴
10³
10²
0
1
2
RAPIDITY
XBL 778-2609

Fig. 36

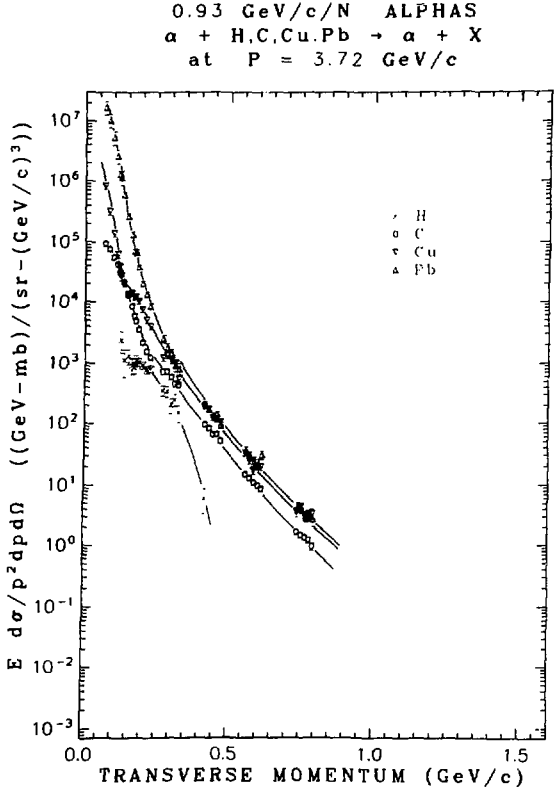
0.93 GeV/c/N ALPHAS
α + H,C,Cu.Pb → α + X
at P = 3.72 GeV/c
E dσ/p²dpdΩ ((GeV-mb)/(sr-(GeV/c)³))
TRANSVERSE MOMENTUM (GeV/c)
H
C
Cu
Pb
XBL 778-9782

Fig. 37

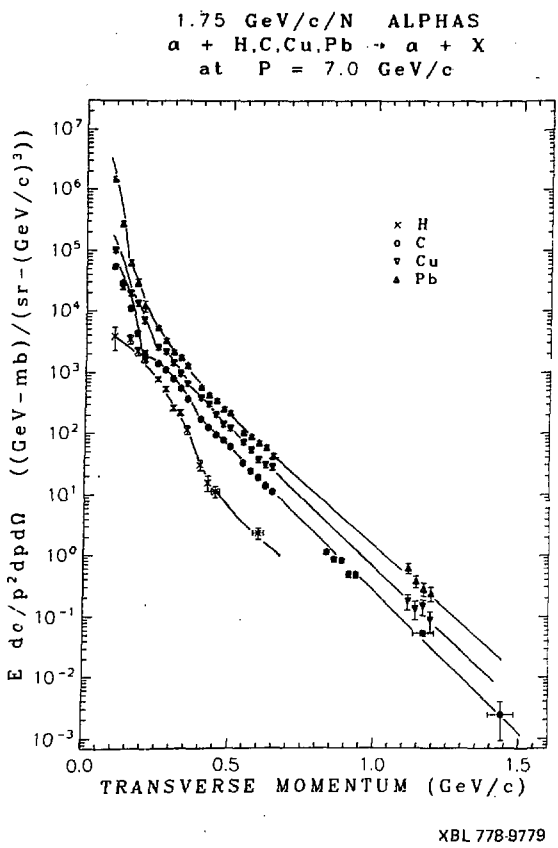
1.75 GeV/c/N ALPHAS
a + H,C,Cu,Pb → a + X
at P = 7.0 GeV/c
E dσ/p²dpdΩ ((GeV-mb)/(sr-(GeV/c)³))
TRANSVERSE MOMENTUM (GeV/c)
H
C
Cu
Pb
XBL 778-9779

Fig. 38

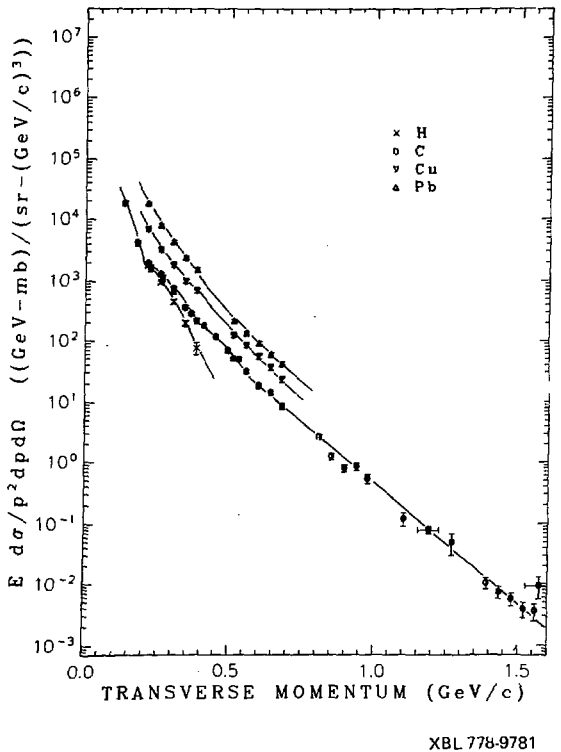
2.88 GeV/c/N ALPHAS
α + H,C,Cu,Pb → α + X
at P = 11.5 GeV/c
E dσ/p²dpdΩ ((GeV-mb)/(sr-(GeV/c)³))
TRANSVERSE MOMENTUM (GeV/c)
H
C
Cu
Pb
XBL 778-9781

Fig. 39

40 shows the data for 1.75 GeV/c/N alphas separately for the four targets. At lower p_T diffraction features are prominent, and at large p_T the dependence on p_T appears to be exponential.

The transverse momentum distributions of protons at several values of momentum for the reaction 2.88 GeV/c/N α + C → p + X are shown in Fig. 41. At p = 2 GeV/c, well below the peak momentum, the p_T distribution is relatively flat. At the projectile velocity (p = 2.88 GeV/c) the distribution has two apparent regions; for $p_T \leq 0.2$ GeV/c the distribution is approximately gaussian with a width of 55 MeV/c, and for $p_T \geq 0.2$ GeV/c it is approximately exponential with an inverse slope of -173 MeV/c. Nearly the same exponential slope appears at high momenta also. Similar features are observed in transverse momentum distributions of the deuterons (Fig. 42), ^{3}He (Fig. 43), and ^{3}H.

The data for the reaction 2.88 GeV/c/N α + C → p + X seen in Figs. 28 and 41 are summarized in yet another way in Fig. 44. Contours of constant invariant cross section are plotted on the rapidity-transverse momentum plane. The countours were obtained by finding the p and p_T where the curves drawn in Figs. 28 and 41 reach fixed values of the cross section. These points were plotted on the (Y, p_T) plane and then the points for a given cross section were joined with a smooth curve. The mirror image in p_T was added for symmetry, and the scales were adjusted so that a distribution which is isotropic in momentum will give circular contours for small momenta in the frame in which the distribution is isotropic.

The highest contours in this plot clearly indicate the dominance of projectile fragmentation in our data. However we can see that, even for these highest contours, the distribution is not exactly isotropic, i.e.

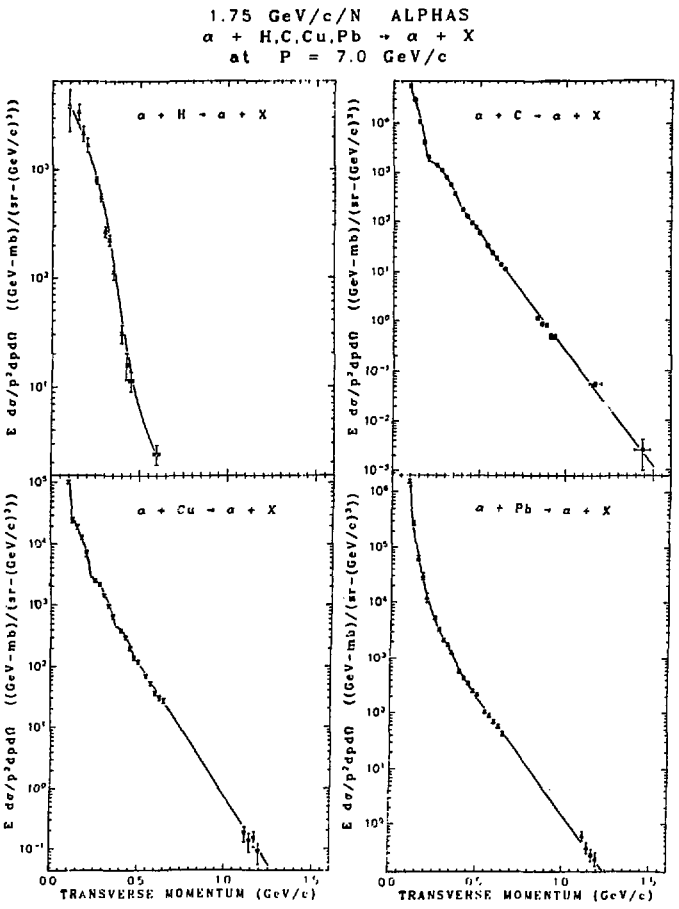
1.75 GeV/c/N ALPHAS
α + H,C,Cu,Pb → α + X
at P = 7.0 GeV/c
α + H → α + X
α + C → α + X
α + Cu → α + X
α + Pb → α + X
E dσ/p²dpdΩ ((GeV-mb)/(sr-(GeV/c)³))
TRANSVERSE MOMENTUM (GeV/c)

Fig. 40

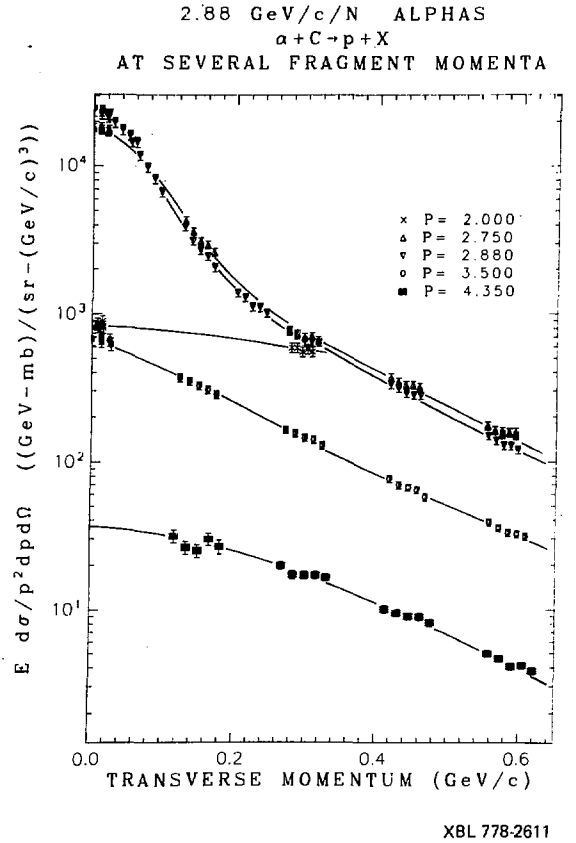

XBL 778-2611

Fig. 41

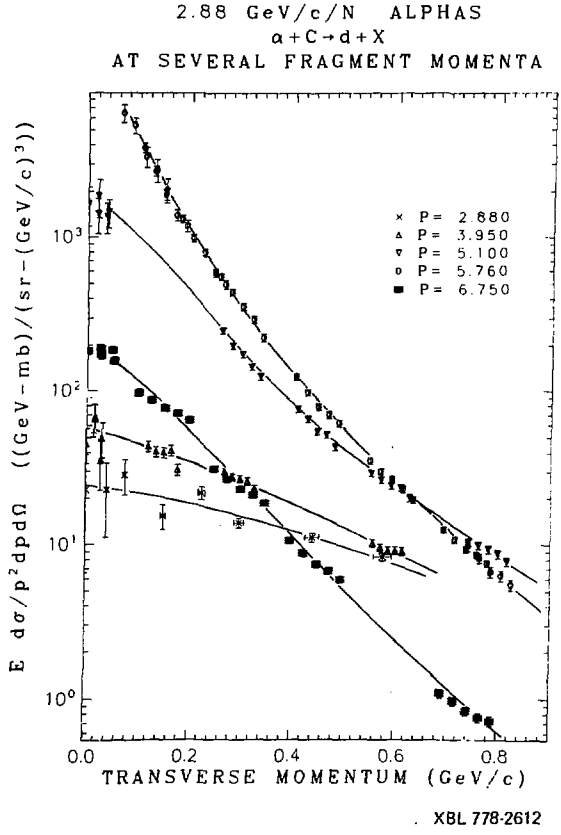
2.88 GeV/c/N ALPHAS
α+C→d+X
AT SEVERAL FRAGMENT MOMENTA
× P= 2.880
△ P= 3.950
▽ P= 5.100
○ P= 5.760
■ P= 6.750
E dσ/p²dpdΩ ((GeV-mb)/(sr-(GeV/c)³))
10³
10²
10¹
10⁰
0.0
0.2
0.4
0.6
0.8
TRANSVERSE MOMENTUM (GeV/c)
XBL 778-2612

Fig. 42

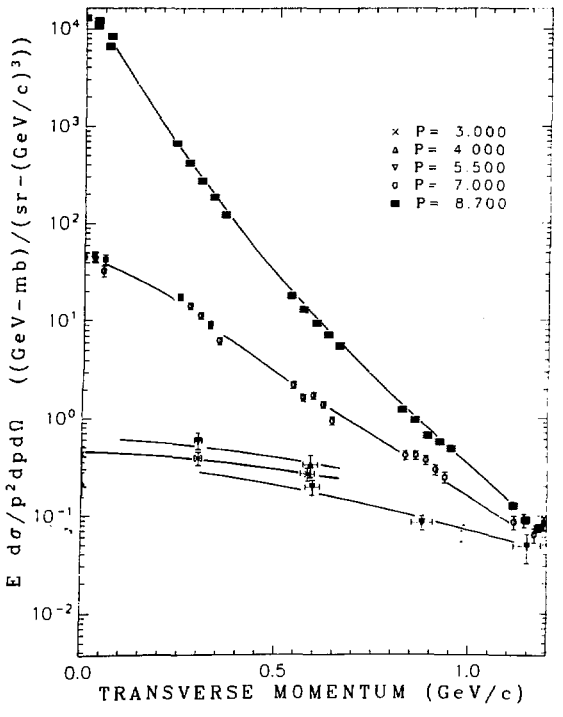

XBL 778-2613

Fig. 43

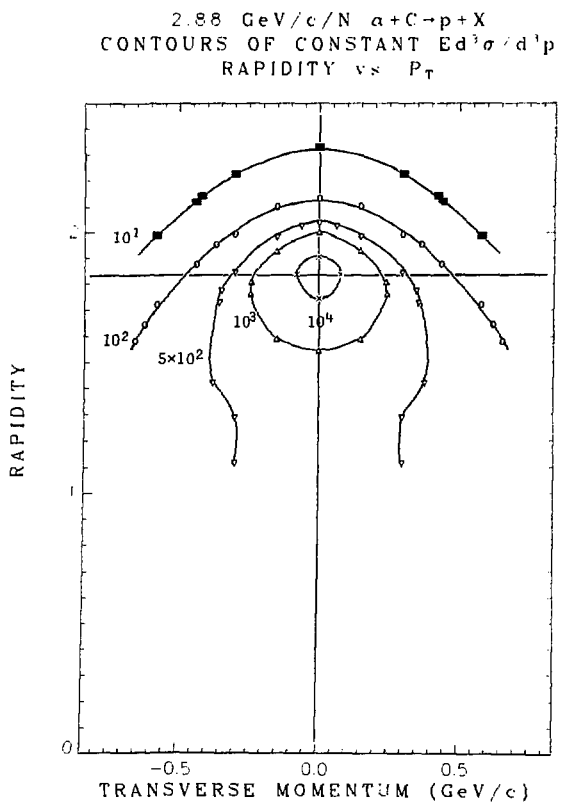

XBL 779-2457

Fig. 44

not even out to p_T = 0.1 GeV/c. It is apparently broader in the backward and transverse directions than in the forward (large rapidity) direction. The intermediate cross section contours indicate the broad central region which is relatively flat in Y and p_T. And the lowest cross section contours at large transverse momenta indicate the kinematic limitation of longitudinal momentum at large p_T, and possibly a source of protons in the central region of intermediate rapidity. This contour plot is a powerful way of summarizing the data and aiding our physical intuition.

B. Limiting Fragmentation

We now turn to a determination of the degree and range (in beam energy, transverse momentum p_T, and projectile frame longitudinal momentum p_L^{PROJ}) of validity of the hypothesis of limiting fragmentation in our data. The transverse momentum distributions of beam velocity protons produced by our three energies of alpha beams incident on a carbon target are shown in Fig. 45 and again in Fig. 46 in a reduced p_T range. There is no apparent energy dependence of the invariant cross section between 1.75 and 2.88 GeV/c/N in these distributions; however the 0.93 GeV/c/N peak is approximately 15% lower, while at p_T = 0.2 all three energies have the same cross section, indicating that the distribution is broader at 0.93 GeV/c/N. The broader distribution at 0.93 GeV/c/N is seen again for the deuteron p_T distribution in Fig. 47. On the other hand, the transverse momentum distributions of ^{3}H shown in Fig. 48 show the opposite energy dependence from that of protons. Namely the ^{3}H distribution peaks at a lower value and is broader with increasing beam energy.

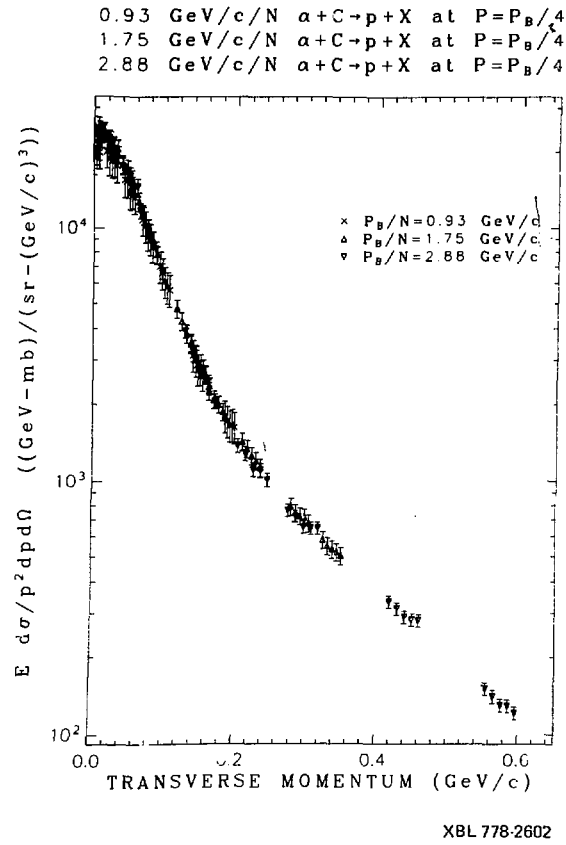
0.93 GeV/c/N α+C→p+X at P=P_B/4
1.75 GeV/c/N α+C→p+X at P=P_B/4
2.88 GeV/c/N α+C→p+X at P=P_B/4
× P_B/N=0.93 GeV/c
△ P_B/N=1.75 GeV/c
▽ P_B/N=2.88 GeV/c
E dσ/p²dpdΩ ((GeV-mb)/(sr-(GeV/c)³))
10⁴
10³
10²
0.0
0.2
0.4
0.6
TRANSVERSE MOMENTUM (GeV/c)
XBL 778-2602

Fig. 45

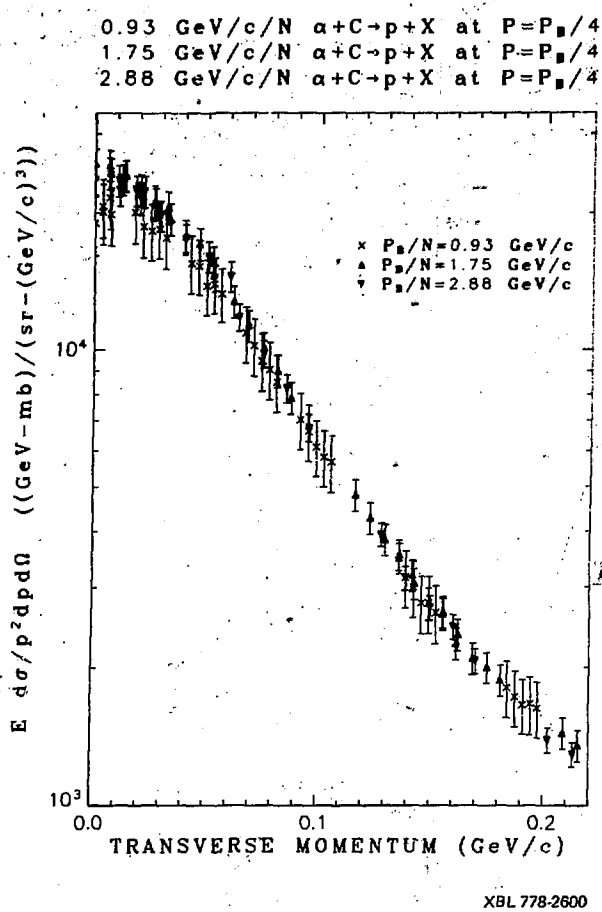
0.93 GeV/c/N α+C→p+X at P=P_B/4
1.75 GeV/c/N α+C→p+X at P=P_B/4
2.88 GeV/c/N α+C→p+X at P=P_B/4
× P_B/N=0.93 GeV/c
▲ P_B/N=1.75 GeV/c
▼ P_B/N=2.88 GeV/c
E dσ/p²dpdΩ ((GeV-mb)/(sr-(GeV/c)³))
10⁴
10³
0.0
0.1
0.2
TRANSVERSE MOMENTUM (GeV/c)
XBL 778-2600

Fig. 46

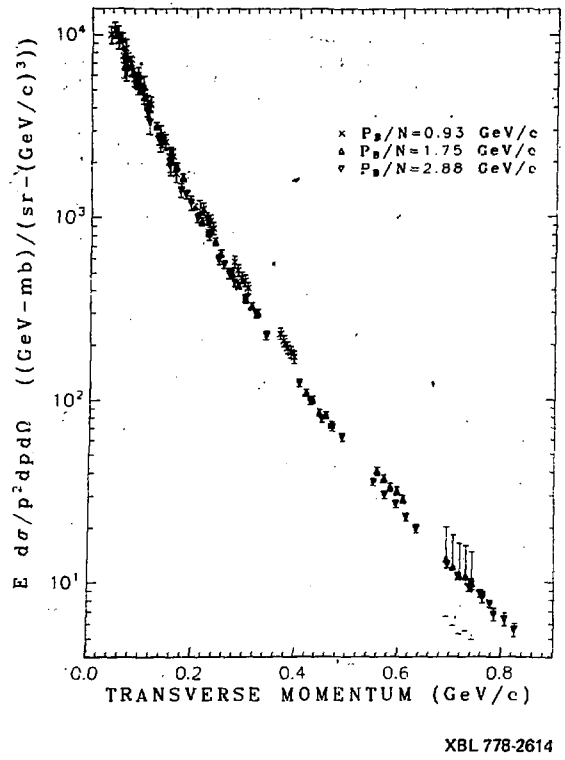

XBL 778-2614

Fig. 47

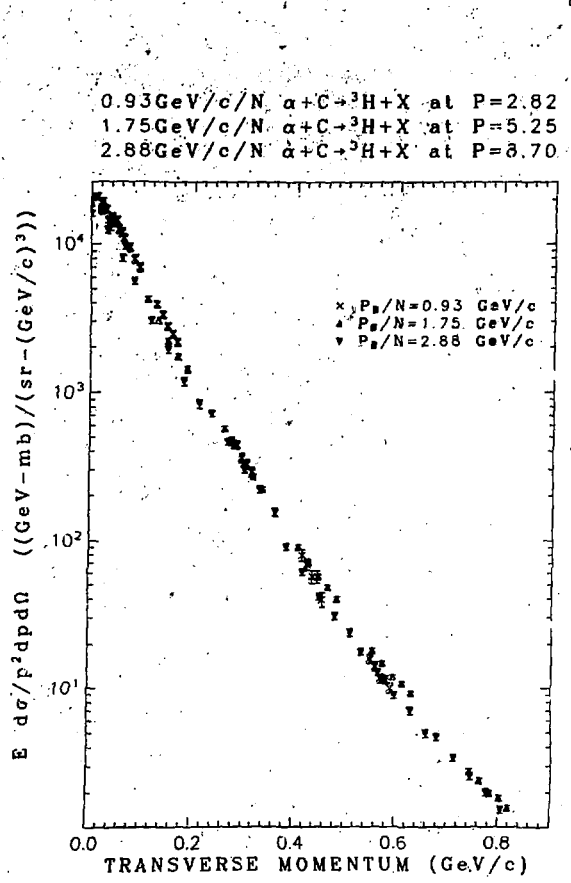

XBL 778-2615

Fig. 48

The projectile rest frame longitudinal momentum distributions of protons at $p_T = 0$ for our three energies of alpha beams incident on a carbon target are shown in Fig. 49, and again in Fig. 50 for $p_L^{PROJ} > 0$ only. Fig. 51 shows the results for $p_T = 0.3$ GeV/c. In both cases, the 0.93 GeV/c/N data fall below the others beginning near $p_L^{PROJ} = 0.2$ GeV/c. At $p_T = 0$ the two higher energies agree within errors out to $p_L^{PROJ} = 0.4$ GeV/c, while at $p_T = 0.3$ GeV/c, the 1.75 GeV/c/N data begin to fall below the 2.88 GeV/c/N data near $p_L^{PROJ} = 0.3$ GeV/c. For $p_L^{PROJ} < 0$ the cross section falls with increasing beam energy.

Limiting fragmentation is thus verified within experimental errors (±7-10%) out to $p^{PROJ} = 0.4$ GeV/c in the energy range 1-2 GeV/N. The contrast between limiting fragmentation and scaling in this energy range may be seen by comparing the p_L^{PROJ} distributions for protons from our three energies of alpha beams incident on a carbon target in Fig. 49 with the distributions in the scaling variable $x' = p_L^{cm}/p_{max}^{cm}$, for the same data as shown in Fig. 52.

This plot also indicates that the faster fall-off with p_L^{PROJ} at large p_L^{PROJ} for the lower energy beams may be due to the constraint imposed by the available phase space.

C. Projectile Frame Anisotropy

In order to determine whether the sudden approximation applies, we can examine the fragment momentum distributions in the projectile rest frame to see if they are isotropic.

First we examine the forward-backward symmetry. Fig. 53 shows the distribution of the longitudinal momentum in the projectile frame, p_L^{PROJ},

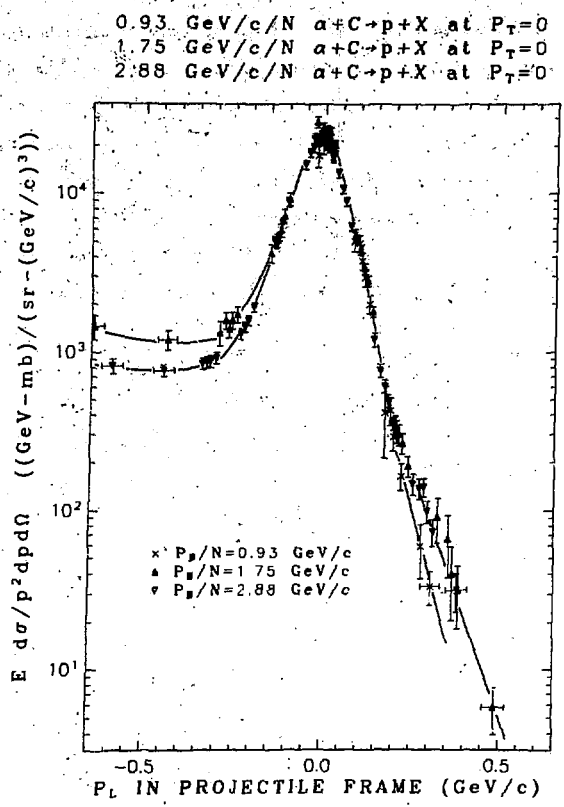

XBL 778-2610

Fig. 49

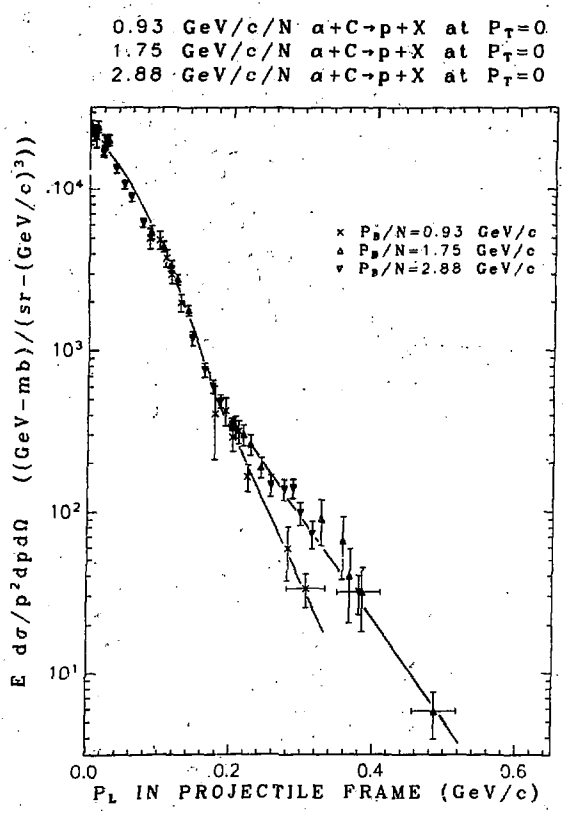
0.93 GeV/c/N α+C→p+X at P_T=0
1.75 GeV/c/N α+C→p+X at P_T=0
2.88 GeV/c/N α+C→p+X at P_T=0
E dσ/p²dpdΩ ((GeV-mb)/(sr-(GeV/c)³))
10⁴
10³
10²
10¹
× P_B/N=0.93 GeV/c
▲ P_B/N=1.75 GeV/c
▼ P_B/N=2.88 GeV/c
0.0
0.2
0.4
0.6
P_L IN PROJECTILE FRAME (GeV/c)
XBL 778-2603

Fig. 50

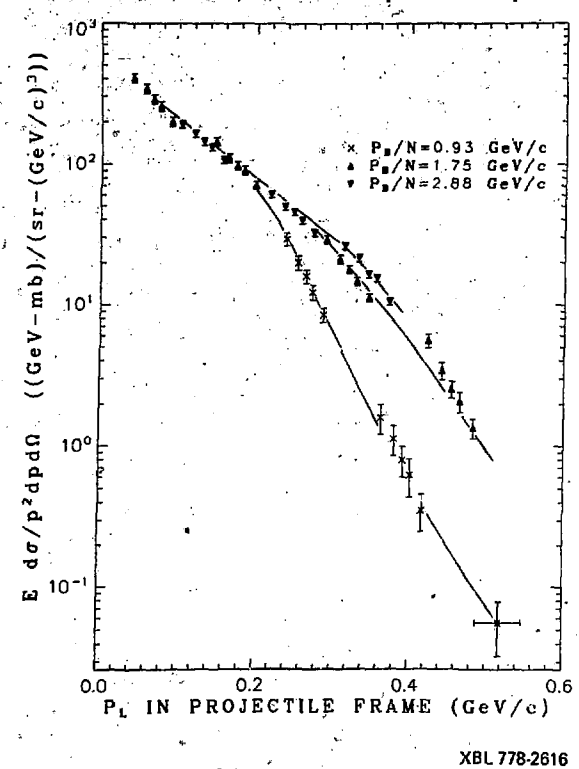
0.93 GeV/c/N α+C→p+X at P_T=.3
1.75 GeV/c/N α+C→p+X at P_T=.3
2.88 GeV/c/N α+C→p+X at P_T=.3
P_B/N=0.93 GeV/c
P_B/N=1.75 GeV/c
P_B/N=2.88 GeV/c
E dσ/p²dpdΩ ((GeV-mb)/(sr-(GeV/c)³))
P_L IN PROJECTILE FRAME (GeV/c)
10³
10²
10¹
10⁰
10⁻¹
0.0
0.2
0.4
0.6
XBL 778-2616

Fig. 51

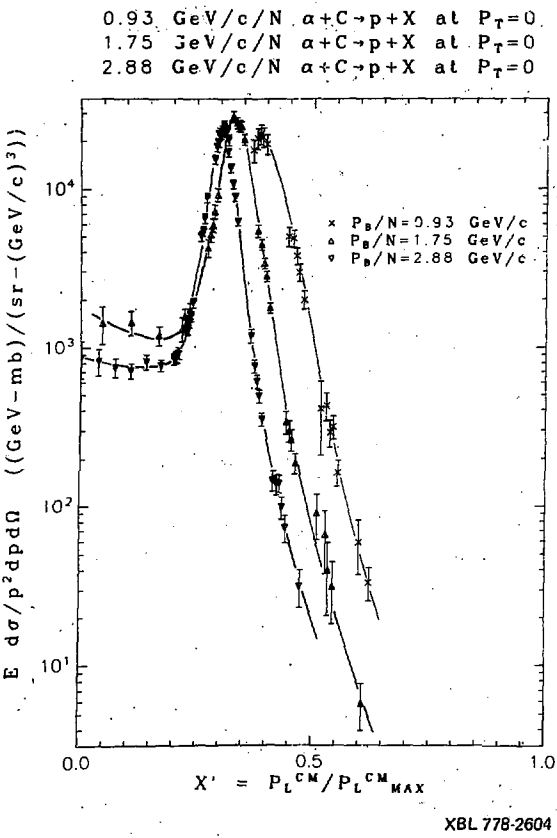
0.93 GeV/c/N α+C→p+X at P_T=0
1.75 GeV/c/N α+C→p+X at P_T=0
2.88 GeV/c/N α+C→p+X at P_T=0
P_B/N=0.93 GeV/c
P_B/N=1.75 GeV/c
P_B/N=2.88 GeV/c
E dσ/p²dpdΩ ((GeV-mb)/(sr-(GeV/c)³))
10⁴
10³
10²
10¹
0.0
0.5
1.0
X' = P_L^CM/P_L^CM_MAX
XBL 778-2604

Fig. 52

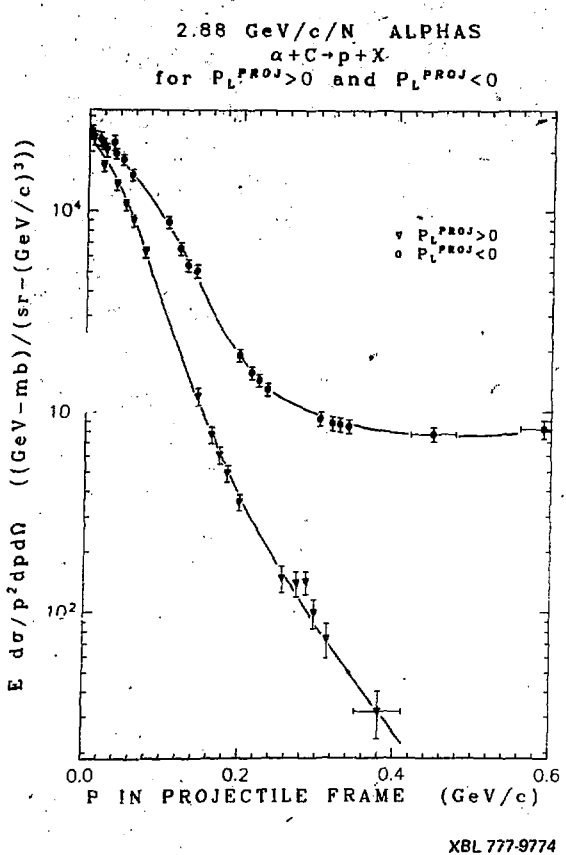
2.88 GeV/c/N ALPHAS
α+C→p+X
for $P_L^{PROJ}>0$ and $P_L^{PROJ}<0$
$E\,d\sigma/p^2dpd\Omega$ ((GeV-mb)/(sr-(GeV/c)³))
10^4
10
10^2
▽ $P_L^{PROJ}>0$
○ $P_L^{PROJ}<0$
0.0
0.2
0.4
0.6
P IN PROJECTILE FRAME (GeV/c)
XBL 777-9774

Fig. 53

for $p_L^{PROJ} > 0$ and $p_L^{PROJ} < 0$ in the reaction 2.88 GeV/c/N α + C → p + X at $p_T = 0$. The $p_L^{PROJ} < 0$ data is lower even at small p_L^{PROJ}. Similar results are shown for deuterons in Fig. 54 and tritons in Fig. 55 from 1.75 GeV/c/N alphas on carbon. Forward-backward symmetry is clearly violated, especially for the lighter fragments.

Forward-transverse symmetry may be examined in Figs. 56-60. Fig. 56 shows the p_L^{PROJ} distribution at $p_T = 0$ and the p_T distribution at $p_L^{PROJ} = 0$ for protons from 1.75 GeV/c/N alphas on carbon. Fig. 57 shows the same distributions for 2.88 GeV/c/N alphas on carbon. The same distributions for deuterons, tritons, and ^{3}He are shown in Figs. 58, 59, and 60 respectively for 1.75 GeV/c/N alphas on carbon. In each case the p_T distributions are much broader and symmetry is violated for $p_L^{PROJ} > 0.075$ GeV/c/N. Clearly the sudden approximation[10] is not valid and the effects of the scattering of the projectile and its fragments by the target must be taken into account.

D. Target Dependence

The dependence of the invariant cross sections on the target material at $p_T = 0$ has already been crudely shown in Figs. 32-36. In order to get a more quantitative measure of this dependence we have fit the data for the carbon, copper, and lead targets to a dependence of the form A_T^N where A_T is the amonic number of the target material and the exponent N is determined from the fit. We may expect $N \leq 1/3$ for peripheral processes where the alpha interacts with the circumference of the target, $N = 2/3$ for processes in which the alpha interacts with the surface area of the target and $N = 1$ when the entire volume contributes. The target dependence N is plotted as a function of fragment momentum at

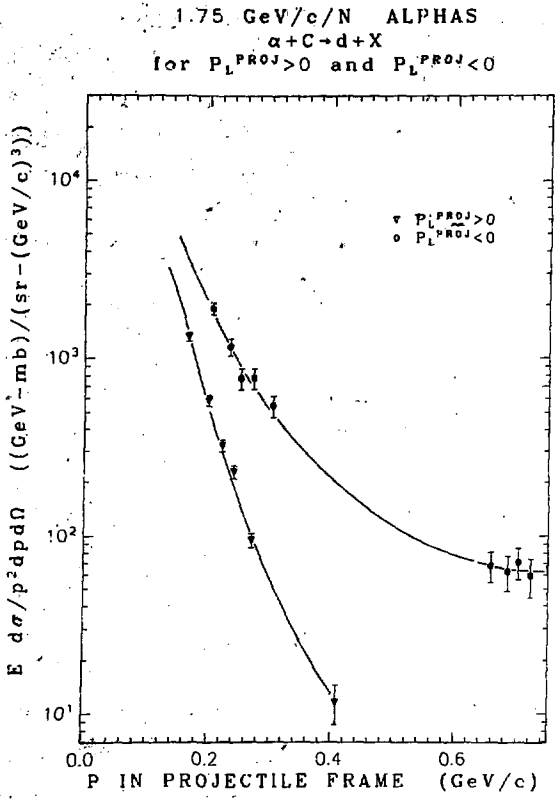

XBL 777-9769

Fig. 54

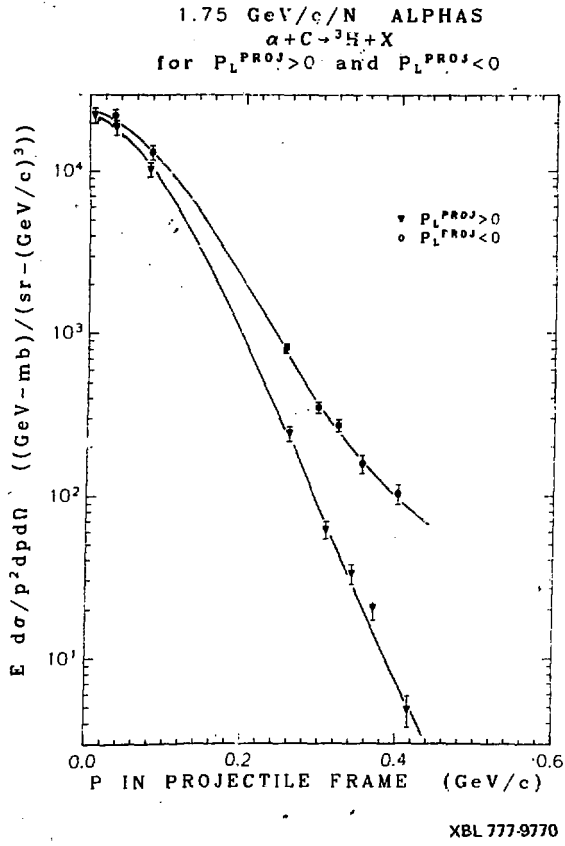
1.75 GeV/c/N ALPHAS
$\alpha + C \rightarrow {}^{3}H + X$
for $P_L^{PROJ} > 0$ and $P_L^{PROJ} < 0$
E dσ/p²dpdΩ ((GeV-mb)/(sr-(GeV/c)³))
10^4
10^3
10^2
10^1
▼ $P_L^{PROJ} > 0$
○ $P_L^{PROJ} < 0$
0.0
0.2
0.4
0.6
P IN PROJECTILE FRAME (GeV/c)
XBL 777-9770

Fig. 55

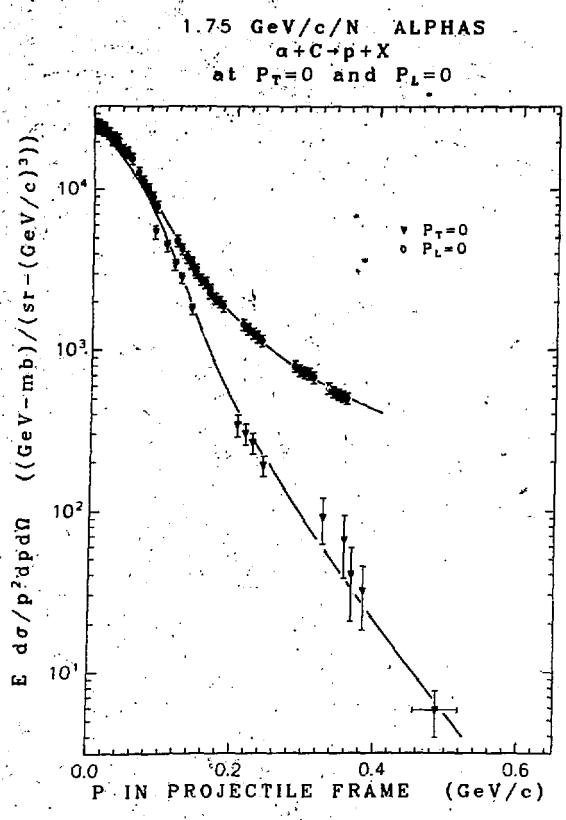
1.75 GeV/c/N ALPHAS
α+C→p+X
at $P_T=0$ and $P_L=0$
$P_T=0$
$P_L=0$
$E\,d\sigma/p^2dpd\Omega$ ((GeV-mb)/(sr-(GeV/c)³))
10^4
10^3
10^2
10^1
0.0
0.2
0.4
0.6
P IN PROJECTILE FRAME (GeV/c)
XBL 777-9772

Fig. 56

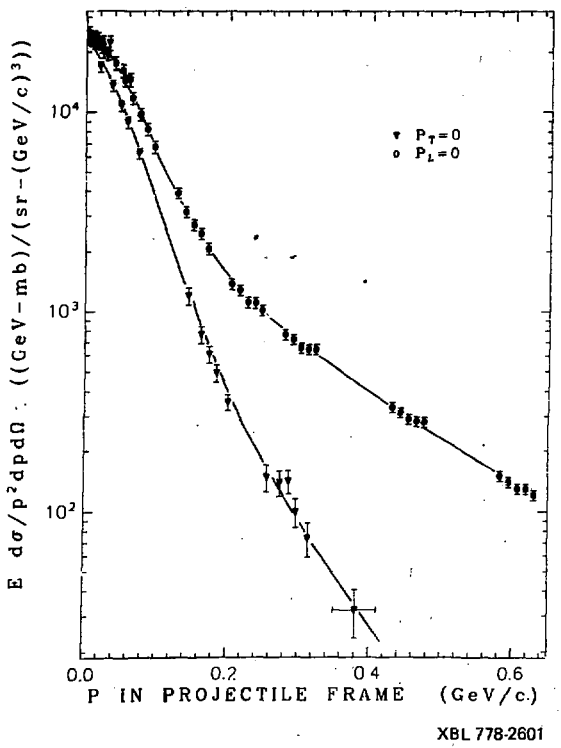
2.88 GeV/c/N ALPHAS
α+C→p+X
at $P_T=0$ and $P_L=0$
$E\ d\sigma/p^2dpd\Omega$: ((GeV-mb)/(sr-(GeV/c)^3))
10^4
10^3
10^2
$P_T=0$
$P_L=0$
0.0
0.2
0.4
0.6
P IN PROJECTILE FRAME (GeV/c.)
XBL 778-2601

Fig. 57

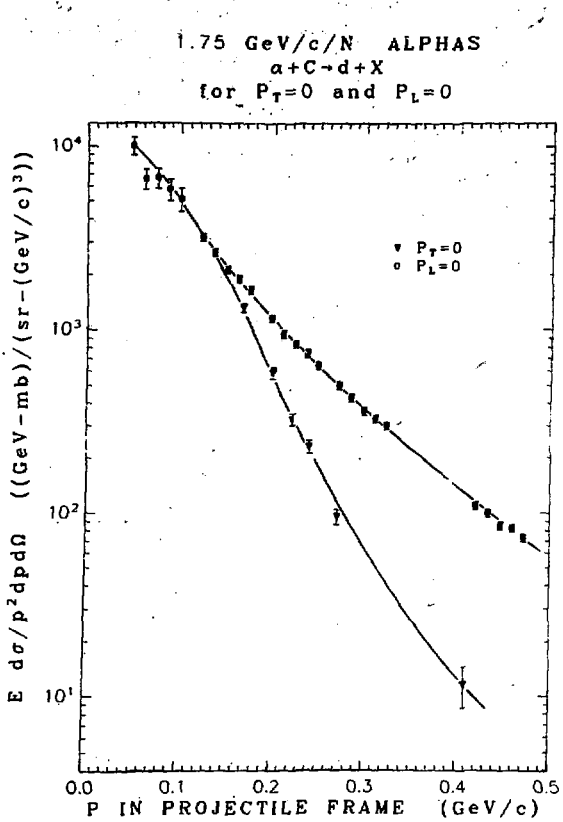

XBL 777-9771

Fig. 58

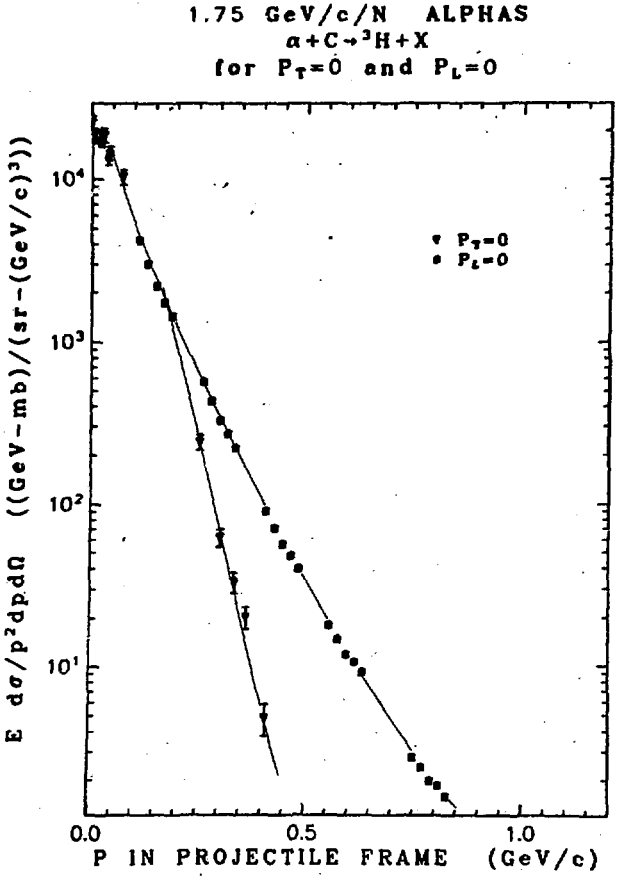
1.75 GeV/c/N ALPHAS
α+C→³H+X
for P_T=0 and P_L=0
E dσ/p²dpdΩ ((GeV-mb)/(sr-(GeV/c)³))
10⁴
10³
10²
10¹
P_T=0
P_L=0
0.0
0.5
1.0
P IN PROJECTILE FRAME (GeV/c)

Fig. 59

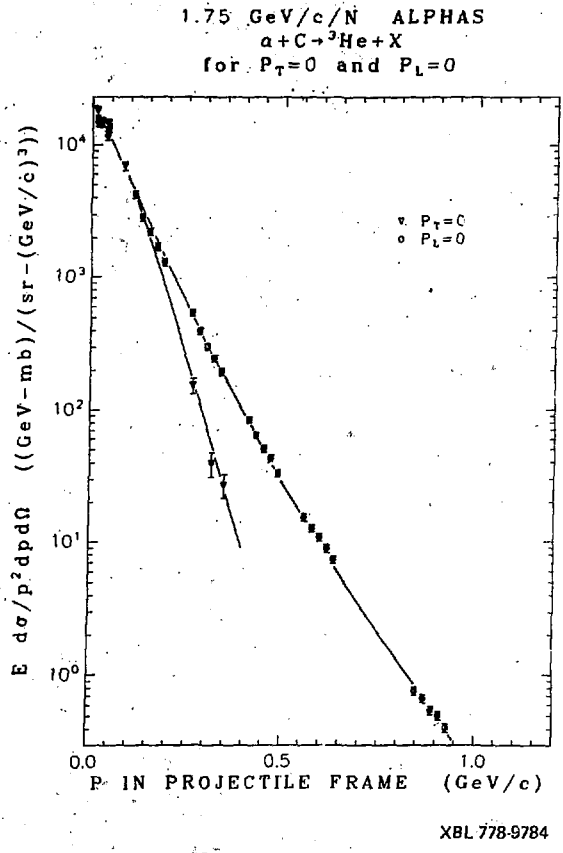
1.75 GeV/c/N ALPHAS
a+C→³He+X
for P_T=0 and P_L=0
E dσ/p²dpdΩ ((GeV-mb)/(sr-(GeV/c)³))
10⁴
10³
10²
10¹
10⁰
P_T=0
P_L=0
0.0
0.5
1.0
P IN PROJECTILE FRAME (GeV/c)
XBL 778-9784

Fig. 60

$p_T = 0$ for the reactions 2.88 GeV/c/N $\alpha + A_T \rightarrow p$, d, ^3H, ^3He in Fig. 61. The results for the same reactions at $p_T = 0.3$ GeV/c are shown in Fig. 62. And the transverse momentum dependence of N for fragments at the beam velocity is shown in Fig. 63.

For protons at $p_T = 0$ and near or beyond the beam velocity we find a nearly constant value of $N = 0.27$, indicating peripheral production and approximate factorization of the target dependence in this region. For the heavier fragments at 0° and at the projectile velocity N is smaller yet, for example N = 0.12 for ^3H and ^3He. At lower momenta the value of N is higher, in fact for ^3H and ^3He it reaches N = 1.4 at p = 1.5 GeV/c. We also find that n rises with p_T (Figs. 62 and 63), indicating that a larger range of impact parameters contributes to events with larger momentum transfer.

E. Model Comparison

In a more quantitative look at the data we have fit the production of fragments at greater than beam velocity to the form $(1 - X_R)^n$ and compared the results with the predictions of Schmidt and Blankenbecler.[17] They propose a relativistic parton model for the nucleus in which the nucleons play the role of partons. The model predicts, using nucleon-nucleon scattering parameters and a generalized Hulthen wave function, which is characterized by a parameter g, that the fragment spectra at large X_R will have the dependence $(1 - X_R)^n$. The exponent n is determined by the measured (and thus fixed) form of the nucleon-nucleon scattering and by the wave function parameter g, which can be calculated from field theoretic models of the nucleon-nucleon interaction in the nculeus. With alpha particles incident, they predict for protons n = 17, for deuterons

2.88 GeV/c/N α+T→p,d,^{3}H,^{3}He+X
at θ=0 deg
N from fit to A_T^N

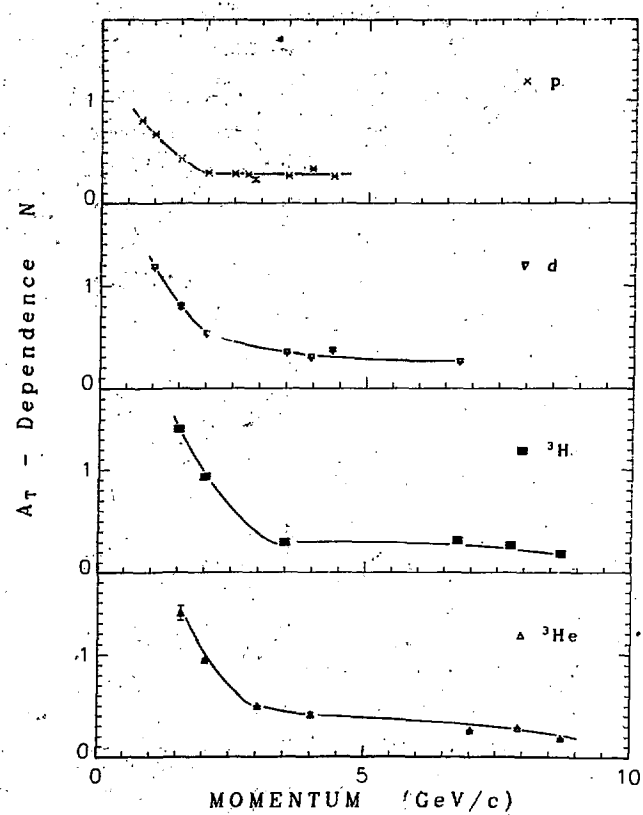

XBL 778-2643

Fig. 61

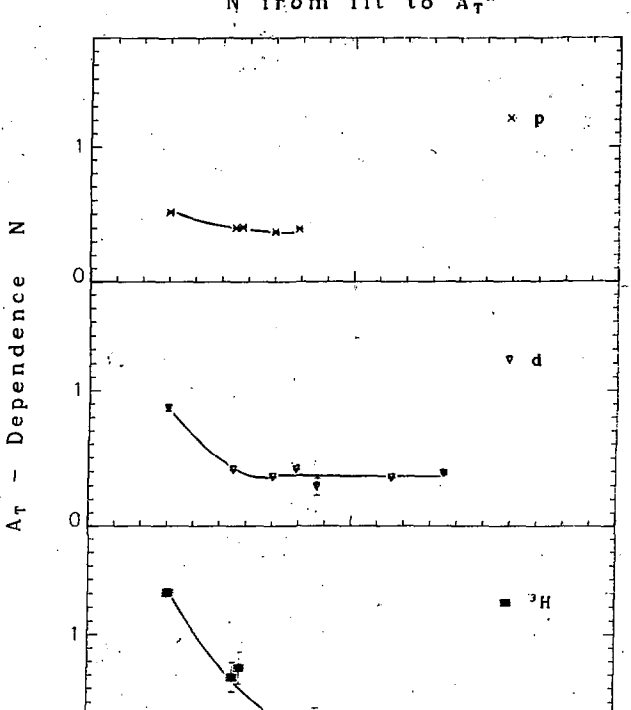
2.88 GeV/c/N α+T→p,d,³H+X
at P_T=.3
N from fit to A_T^N
× p
▽ d
■ ³H
A_T - Dependence N
0
1
0
5
10
MOMENTUM (GeV/c)
XBL 778-2645

Fig. 62

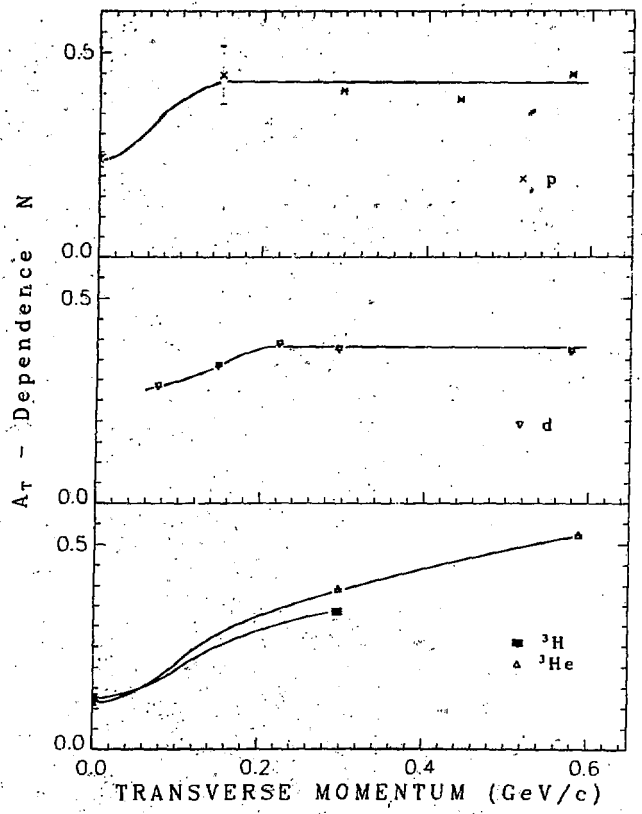

XBL 778-2644

Fig. 63

$n = 11$, and for ^3H and ^3He $n = 5$. Our data and the results of our fits are shown in Figs. 64-67. For the proton production in the reaction $\alpha + C \rightarrow p + X$, we are not able to obtain a good fit for all X_R beyond the quasi-elastic (beam velocity) peak. Rather we find two distinct regions with the break occurring at $p_L^{PROJ} = 0.2$ GeV/c. In Fig. 64 we see that the first region, near to the peak, is fit well by $n = 35$ (± 0.4), and the second (higher X_R) region, where the model should apply, is fit by $n = 15$ (± 6). For 1.75 GeV/c/N alphas (Fig. 65) we obtain $n = 11.3$ (± 0.2) for the high-X_R region. These high X_R results are both consistent with $n = 11.3$, since the error on the 2.88 GeV/c/N data is very large. And the results are inconsistent with $n = 17$. Fitting the high X_R distributions for non-zero p_T we get values of n near 11, decreasing slightly but consistently at larger p_T (Fig. 65). In contrast the model predicts that n should rise with p_T.

For 1.75 GeV/c/N $\alpha + C \rightarrow d + X$ at $p_T = 0$ we obtain $n = 13.2$ (± 3.8) and at $p_T = 0.3$, $n = 9.28$ (± 0.17) where $n = 11$ is predicted. The fits to the data are shown in Fig. 66 and large deviations from the data are observed for both fits. For 1.75 GeV/c/N $\alpha + C \rightarrow H + X$ at $p_T = 0$ we obtain $n = 3.9$ (± 0.2), compared with the predicted value $n = 5$, and at $p_T = 0.3$ we obtain $n = 3.54$ (± 0.04). These results may be seen in Fig. 67 and they deviate considerably from the data at $p_T = 0$. For these heavier fragments the onset of the asymptotic region where the model should apply is not clearly seen in our somewhat sparse data at large X_R, so that it is difficult to make a clear test; however the model predictions appear to be consistently too high.

In summary, although the model of Schmidt and Blankenbecler correctly predicts the usefulness of the parameterization of the cross section for

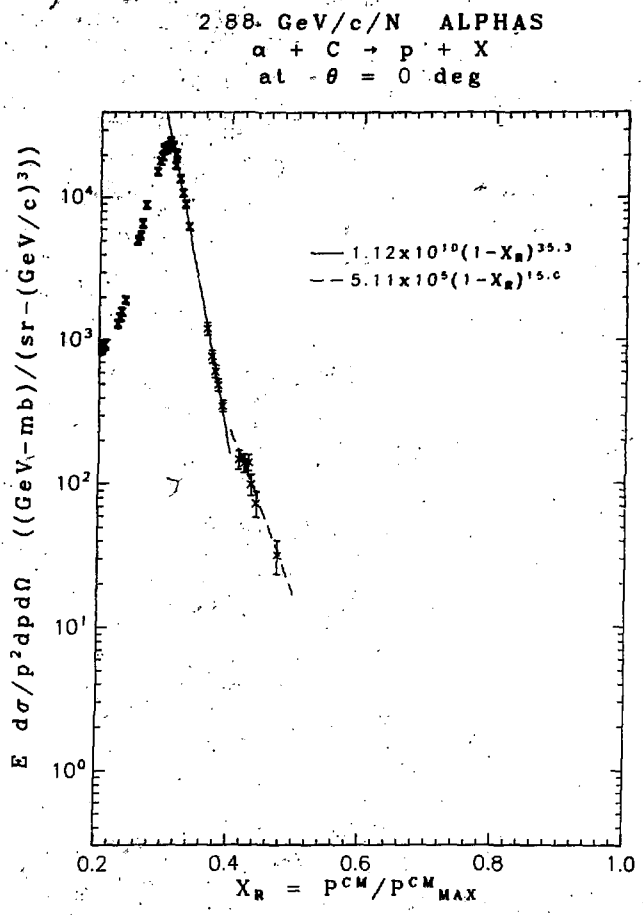

XBL 778-2642

Fig. 64

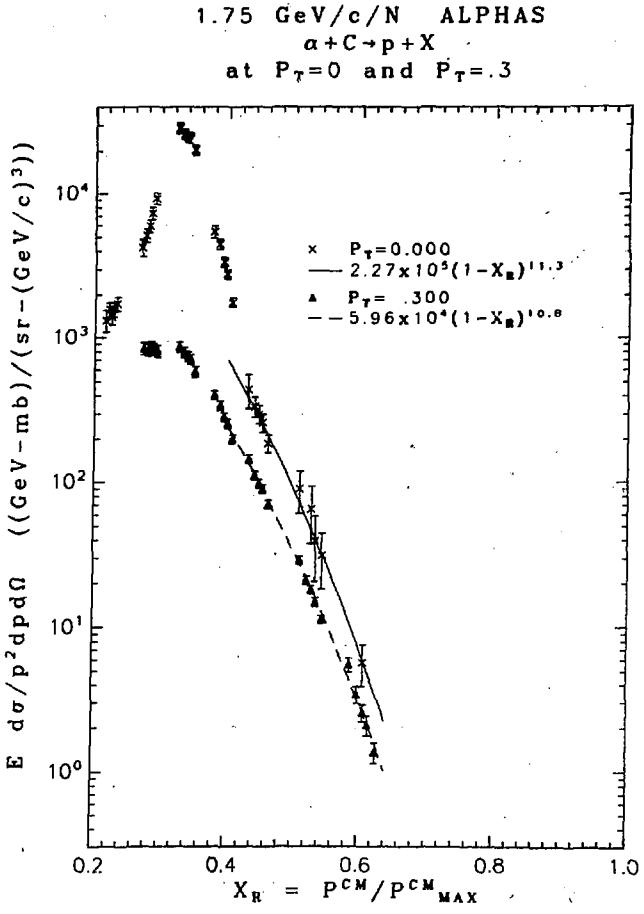
1.75 GeV/c/N ALPHAS
α+C→p+X
at P_T=0 and P_T=.3
E dσ/p²dpdΩ ((GeV-mb)/(sr-(GeV/c)³))
10^4
10^3
10^2
10^1
10^0
× P_T=0.000
—— 2.27x10³(1-X_R)^11.3
▲ P_T= .300
– – 5.96x10⁴(1-X_R)^10.6
0.2
0.4
0.6
0.8
1.0
X_R = P^{CM}/P^{CM}_{MAX}
ABL 778-2647

Fig. 65

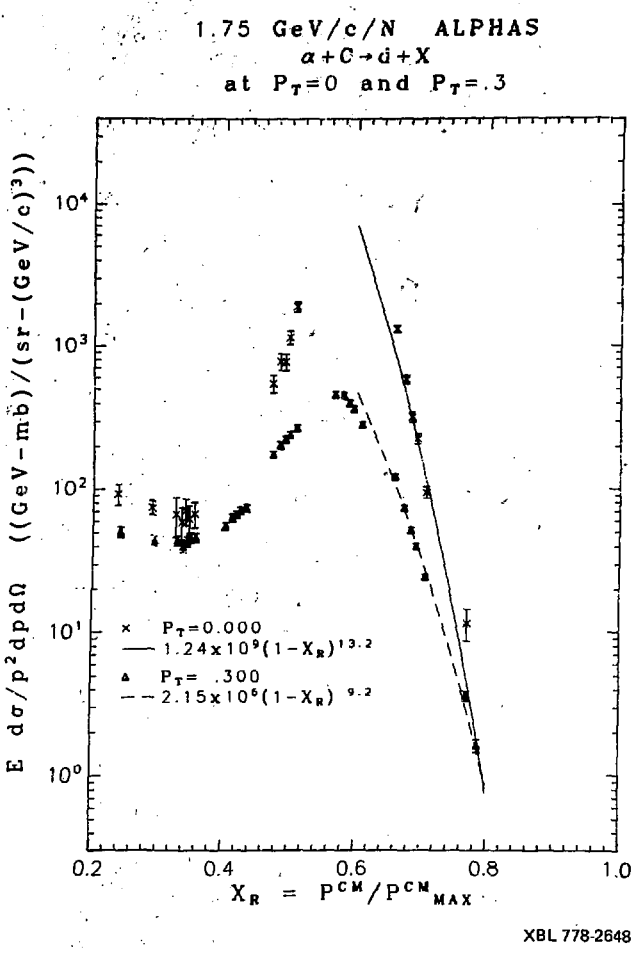
1.75 GeV/c/N ALPHAS
α+C→d+X
at P_T=0 and P_T=.3
E dσ/p²dpdΩ ((GeV-mb)/(sr-(GeV/c)³))
10^4
10^3
10^2
10^1
10^0
× P_T=0.000
1.24x10⁹(1-X_R)^13.2
△ P_T= .300
2.15x10⁶(1-X_R)^9.2
0.2
0.4
0.6
0.8
1.0
X_R = P^{CM}/P^{CM}_{MAX}
XBL 778-2648

Fig. 66

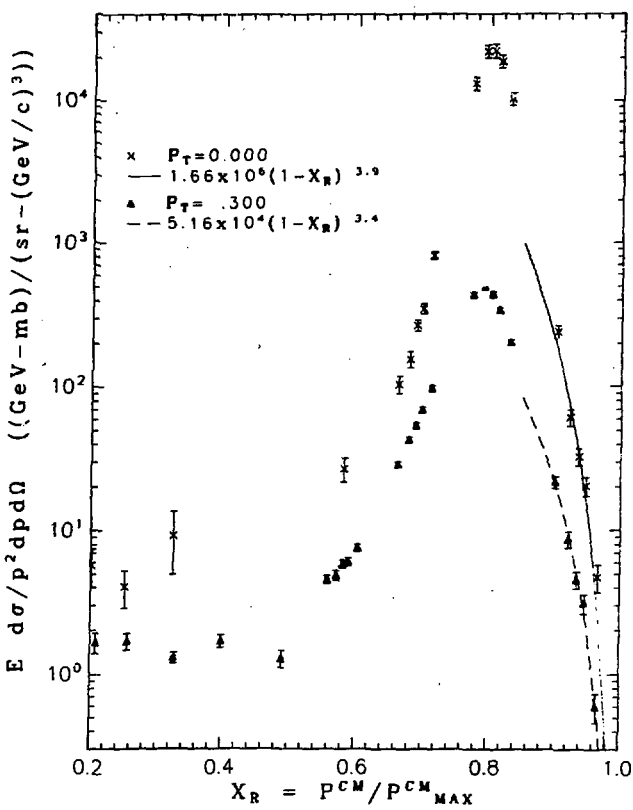
1.75 GeV/c/N ALPHAS
α+C→³H+X
at P_T=0 and P_T=.3
E dσ/p²dpdΩ ((GeV-mb)/(sr-(GeV/c)³))
10⁴
10³
10²
10¹
10⁰
× P_T=0.000
1.66x10⁶(1-X_R)^3.9
▲ P_T= .300
5.16x10⁴(1-X_R)^3.4
0.2
0.4
0.6
0.8
1.0
X_R = P^CM/P^CM_MAX
XBL 778-2646

Fig. 67

the fast forward fragments by $(1 - X_R)^n$, the detailed predictions of the model do not agree with our data.

We have also compared our data with the predictions of the coalescence model.[31] This model predicts the distribution of the heavier fragments by assuming that they are formed through the coalescence of the cascade nucleons within some momentum radius p_0. The radius p_0 is determined by a fit to the data. Fig. 68 shows a comparison of the predictions for the deuteron and ^{3}H-^{3}He spectra obtained from the proton spectrum for 1.75 GeV/c/N alphas incident on carbon. Fig. 69 shows the comparison for the 2.88 GeV/c/N beam. The momentum radius p_0 = 110 MeV/c was chosen to fit the data in the central regions. The model predicts well the relative sizes of the deuteron and ^{3}H-^{3}He cross sections in this region and does surprisingly well on the bulk of the 1.75 GeV/c/N data. For the 2.88 GeV/c/N data it falls below the data in the tails of the fragment distributions and is generally low for the ^{3}H-^{3}He production. Figs. 70 and 71 show that the angular distribution is not well predicted by the model, with the model falling consistently lower than the ^{3}H-^{3}He data. Of course this model is expected to apply only in the central region where the production mechanism is pictured as having two steps: 1) the nuclei break into quasi-free nucleons, 2) these coalesce into the observed isotopes. In the fragmentation peak regions, however, one does not expect the nuclei to totally break apart into free nucleons. Thus in these regions we can expect such a model at best to set a minimum to which other mechanisms must be added.

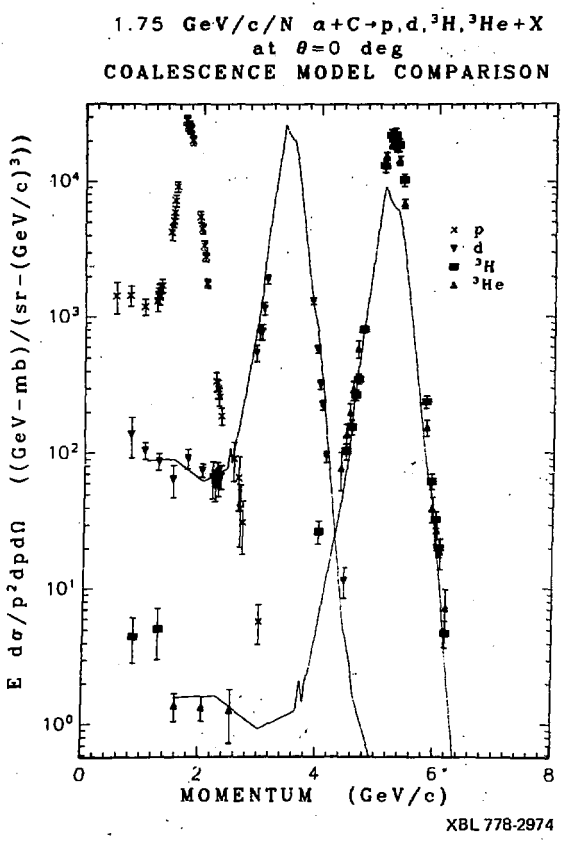
1.75 GeV/c/N α+C→p,d,³H,³He+X
at θ=0 deg
COALESCENCE MODEL COMPARISON
E dσ/p²dpdΩ ((GeV-mb)/(sr-(GeV/c)³))
MOMENTUM (GeV/c)
p
d
³H
³He
XBL 778-2974

Fig. 68

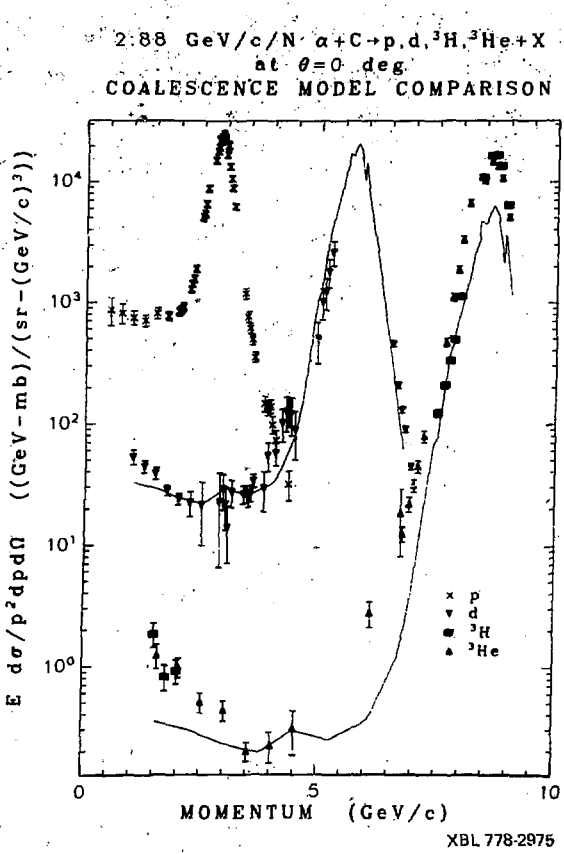
2.88 GeV/c/N α+C→p,d,³H,³He+X
at θ=0 deg.
COALESCENCE MODEL COMPARISON
E dσ/p²dpdΩ ((GeV-mb)/(sr-(GeV/c)³))
MOMENTUM (GeV/c)
p
d
³H
³He
XBL 778-2975

Fig. 69

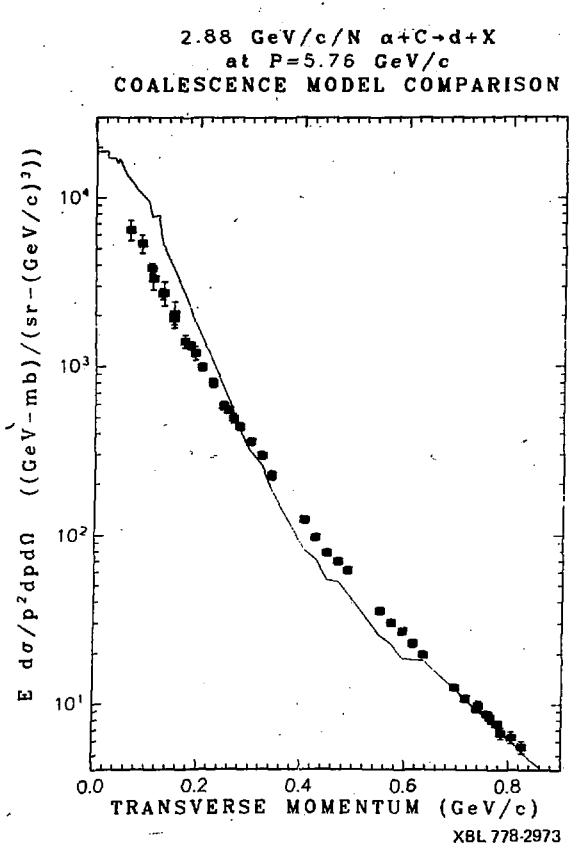
2.88 GeV/c/N α+C→d+X
at P=5.76 GeV/c
COALESCENCE MODEL COMPARISON
E dσ/p²dpdΩ ((GeV-mb)/(sr-(GeV/c)³))
10⁴
10³
10²
10¹
0.0
0.2
0.4
0.6
0.8
TRANSVERSE MOMENTUM (GeV/c)
XBL 778-2973

Fig. 70

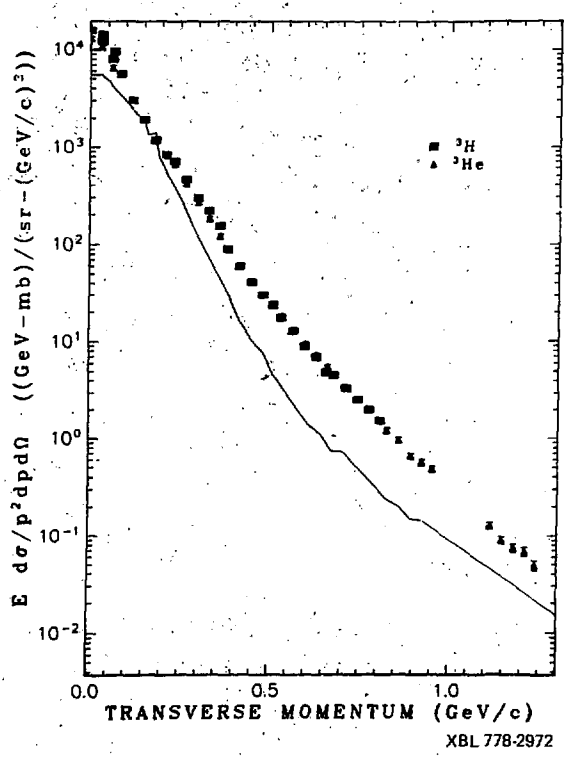
2.88 GeV/c/N α+C→³H,³He+X
at P=8.7 GeV/c
COALESCENCE MODEL COMPARISON
E dσ/p²dpdΩ ((GeV-mb)/(sr-(GeV/c)²))
10⁴
10³
10²
10¹
10⁰
10⁻¹
10⁻²
³H
³He
0.0
0.5
1.0
TRANSVERSE MOMENTUM (GeV/c)
XBL 778-2972

Fig. 71

F. Summary and Conclusion

As yet the longitudinal and transverse momentum distributions measured in this experiment are not predicted by any existing model; however we can point out the dominant features of the data:

1) A sharp fragmentation peak at the projectile velocity and in the forward direction for each fragment of mass less than that of the projectile. The production in these peaks is predominantly peripheral and agrees with limiting fragmentation for beam energies from 1-2 GeV/N and fragment momenta at least to 0.4 GeV/c in the projectile frame. The projectile frame momentum distribution is not isotropic, being broader in the transverse and backward directions than the forward direction. These distributions, at least in the case of protons, appear to be composed of two distinct regions in both the forward and transverse directions with the break occurring at $p^{PROJ} \approx 0.2$ GeV/c. The momentum at which the cross section reaches its peak value at $p_T = 0$ agrees well with what is expected from persistence of velocity, and this peak shifts to lower momenta at larger p_T.

2) Target fragmentation distributions of which we see only the distant tail.

3) A central plateau (for protons) or valley (for the heavier products) with a very shallow angular dependence and approximate target mass dependence of $A_T^{0.4}$ to $A_T^{0.6}$. With increasing beam energy, this region becomes deeper (and of course broader), especially for the heavier fragments.

We can as yet only begin to ask questions about the rich and varied spectra shown above. The wealth of data from this experiment will, we

hope, help us expand our understanding of "high energy" concepts such as limiting fragmentation, particle production mechanisms, nuclear structure, and hadron-hadron interactions in general. It is only by combining the knowledge, insight, and techniques derived from the study of hadrons at all available energies that we are likely to be able to reach a full and concrete understanding of this apparently exptremely complex but, we hope, ultimately simple property of matter we call the strong interaction.

REFERENCES

1. G. F. Chew, Comments Nucl. Part. Phys. 2, 107 (1968).
2. G. F. Chew, "High Energy Heavy Ion Beams as Tests of Nuclear Democracy and as a Tool to Clarify Regge Asymptotic Behavior," LBL Internal Report, March 10, 1972 (unpublished).
3. G. F. Chew, "Large and Small Baryon Numbers in High Energy Collision Theory," LBL Internal Report, May 21, 1973 (unpublished).
4. J. Papp, LBL-3633, Berkeley (1975), Ph.D. Thesis (unpublished).
5. P. J. Lindstrom, D. E. Greiner, H. H. Heckman, Bruce Cork, and F. S. Beiser, LBL-3650, February 1975 (unpublished).
6. D. E. Greiner, P. J. Lindstrom, H. H. Heckman, Bruce Cork, and F. S. Beiser, Phys. Rev. Lett. 35, 152 (1975).
7. M. Gazzaly, Berkeley (1977), Ph.D. Thesis (in preparation).
8. J. Benecke, T. Chou, C. Yang, E. Yen, Phys. Rev. 188, 2159 (1969).
9. G. Belletini, P. L. Braccini, C. Bradaschia, R. Castaldi, T. Del Prete, L. Foa, P. Firomini, P. Laurelli, A. Menzione, M. Valdata, G. Pinocchiara, P. Grannis, D. Green, R. Mustard, R. Thun, Phys. Lett. 45B, 69 (1973).
10. J. V. Lepore and R. J. Riddell, Jr., LBL-3086, July 1974 (unpublished).
11. R. Glauber, Lectures in Theoretical Physics, Boulder, Colorado, 1958, ed. W. E. Britten, L. G. Dunham (Interscience Publishers, Inc., New York, 1959), Vol. I, p. 315.
12. a) L. Bertocchi, A. Tekou, Nuovo Cimento 21A, 223 (1974).
    b) L. Bertocchi, D. Treleani, TH.2203-CERN, 1976 (unpublished).
13. S. Nissen-Meyer, to be published.

14. J. Hüfner, K. Shafer, and B. Schurmann, Phys. Rev. 12C, 1888 (1975).

15. J. Hüfner, and J. Knoll, submitted to Nucl. Phys. A, April 1977.

16. R. P. Feynman, Phys. Rev. Lett. 23, 1415 (1969).

17. I. A. Schmidt and R. Blankenbecler, Phys. Rev. 15D, 3321 (1977).

18. Y. Karant and R. Malfliet, to be published.

19. A. S. Goldhaber, Phys. Lett. 53B, 306 (1974).

20. V. K. Lukyanov and A. I. Titov, Phys. Lett. 57B, 10 (1975).

21. H. W. Bertini, T. A. Gabriel, R. T. Santoro, Phys. Rev. 9C, 522 (1974).

22. J. N. Ginocchio, to be published.

23. M. Danos and R. K. Smith, Jr., to be published.

24. Z. Fraenkel et al., to be published.

25. A. M. Zebelman, A. M. Poskanzer, J. D. Bowman, R. G. Sextro, and V. E. Viola, Jr., Phys. Rev. 11C, 1280 (1975).

26. J. Gosset, H. H. Gutbrod, W. G. Meyer, A. M. Poskanzer, A. Sandoval, R. Stock, and G. D. Westfall, LBL-5820, May 1977, submitted to Phys. Rev. C.

27. H. J. Crawford, P. B. Price, J. Stevenson, and Lance W. Wilson, Phys. Rev. Lett. 34, 329 (1975).

28. A. M. Poskanzer, R. G. Sextro, A. M. Zebelman, H. H. Gutbrod, A. Sandoval, and R. Stock, Phys. Rev. Lett. 35, 1701 (1975).

29. S. Nagamiya, I. Tanihata, S. R. Schnetzer, W. Brückner, L. Anderson, G. Shapiro, H. Steiner, and O. Chamberlain, to be published.

30. G. D. Westfall, J. Gosset, P. J. Johansen, A. M. Poskanzer, W. G. Meyer, H. H. Gutbrod, A. Sandoval, and R. Stock, Phys. Rev. Lett. 37, 1202 (1976).

31. H. H. Gutbrod, A. Sandoval, P. J. Johansen, A. M. Poskanzer, J. Gosset, W. G. Meyer, G. D. Westfall, and R. Stock, Phys. Rev. Lett. 37, 667 (1976).

32. W. Myers, to be published.

33. S. E. Koonin, to be published.

34. A. A. Amsden, G. F. Bertsch, F. H. Harlow, and J. R. Nix, Phys. Rev. Lett. 35, 905 (1975).

35. G. F. Chapline, M. H. Johnson, E. Teller, and M. S. Weiss, Phys. Rev. 8D, 4302 (1973).

36. H. G. Baumgardt, J. U. Schott, Y. Sakamoto, E. Schopper, H. Stöcker, J. Hofmann, W. Scheid, and W. Greiner, Z. Phys. A273, 359 (1975).

37. M. I. Sobel, P. J. Siemens, J. P. Bondorf, H. A. Bethe, Nucl. Phys. A251, 502 (1975).

38. A. R. Bodmer, and C. N. Panos, Phys. Rev. 15C, 1342 (1977).

39. J. P. Bondorf, H. T. Feldmeier, S. Garpman, and E. C. Halbert, Phys. Lett. 65B, 217 (1976).

40. J. A. Jaros, LBL-3849, Berkeley (1975), Ph.D. Thesis (unpublished).

41. J. Cuperus, R. Morgado, IEEE Transactions on Nuclear Science, NS-22, 1561 (1975).

42. J. H. Cobb, HEP/T/55, Oxford (1975), Ph.D. Thesis (unpublished).

43. B. B. Rossi, High Energy Particles (Prentice-Hall, New York, 1952).

44. W. H. Barkas and M. J. Berger, Tables of Energy Losses and Ranges of Heavy Charged Particles, NASA SP-3013, 1964 (unpublished).

45. O. Benary, L. R. Price, and G. Alexander, UCRL-2000 NN, Berkeley, 1975 (unpublished).

46. E. M. Henley in Isospin in Nuclear Physics, ed. D. H. Wilkinson, North Holland Publishing Company, Amsterdam, 1969.

APPENDIX I

Ion Chamber Calibration

The ion chamber was calibrated with beams of 1.75 GeV/c/N and 2.88 GeV/c/N $^{12}C^{+6}$ counted directly with a scintillation counter. This straightforward procedure was slightly complicated by three facts:

1) The Bevatron's pulsing magnetic field, motor generators and other apparatus induced in the chamber and its signal cable a significant amount of noise which had to be recorded and subtracted.

2) The ion chamber had only a 1/4" thick active region and thus was of somewhat low sensitivity.

3) At high incident rates the photomultiplier and its electronics have significant deadtime and thus do not count with complete efficiency.

In order to determine the background noise, the ion chamber readings were recorded for about 20 pulses with the beam plug in the channel. During the calibrations incident rates of 5×10^4 to 1.0×10^6 C^{+6} per Bevatron pulse were used for about 200 pulses.

In order to determine the ion chamber calibration all the data were fit to a formula which takes into account the deadtime τ in the counter and electronics. For N particles per second counted, the deadtime per second is $N\tau$, so if I particles per second are incident the number per second not counted is $N\tau I$, the number counted is $N = I - N\tau I$ and $I/N = 1 + \tau I$. If a charge Q is collected on capacitance C in one second, producing voltage V to be read by the digital voltmeter, then $Q = CV \propto I$, so we may fit the data to the formula $Q/N = a + bQ$ and obtain the ion chamber calibration factor $K = 1/a$ (given in Table 3 in alphas/10^{-11} coulombs).

Figure A1 is a scatter plot of Q/N vs. Q for individual pulses of 1.75 GeV/c/N C^{+6}. The fit determines K with a standard deviation of ±1%.

The results of the calibrations are shown in Fig.A2 superimposed on a plot of dE/dx in argon vs. kinetic energy.[44] No saturation of the signal in the ion chamber relative to the other beam monitors was observed up to rates of 3×10^9 alphas per second, so the Z^2 and velocity dependence of dE/dx should allow us to determine the calibrations for our three energies of alpha-particle beams. The results of this determination, using the 1.75 GeV/c/N C^{+6} calibration as the basis for the calculation, are given in Table 4 in Section III.

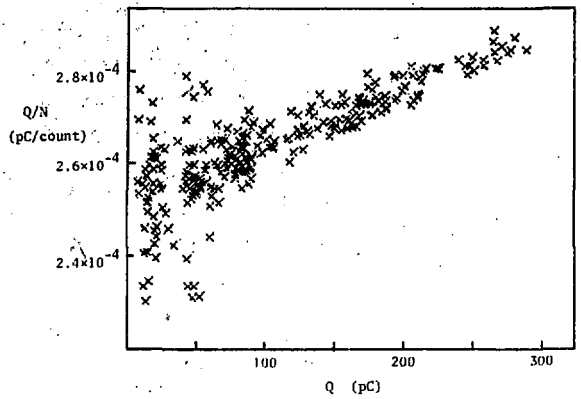

Fig. A1 Ion chamber charge per counted carbon ion vs. ion chamber charge for individual Bevalac pulses. Each pulse is about one second long.

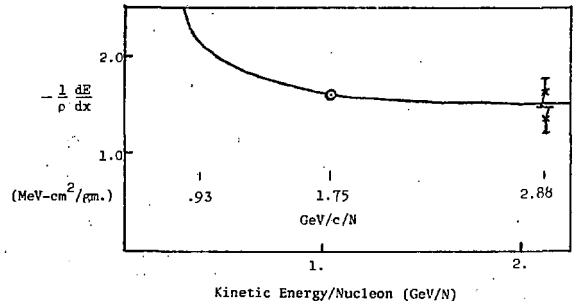

Fig. A2 Energy loss of protons in argon vs. kinetic energy/ nucleon compared with our ion chamber calibration results normalized to the energy loss curve at 1.05 GeV/N (1.75 GeV/c/N).

XBL 779-2469

APPENDIX II

Monitor Telsocope Calibration

The ionization chamber (IC) and secondary emission monitor (SEM) are sensitive to the entire beam coming down the channel; however the scintillation counter monitor telescopes M1, M2, and M3 are sensitive only to the beam incident on the target and are thus the most reliable beam monitors for cross section calculations. In order to obtain an absolute calibration of the telescope monitors at each energy and for each target we used the ion chamber and the "large" targets, which are made of material identical to the standard targets but are large enough to intercept the entire incident beam.

Let us define the calibration factor K for a beam monitor as the number of incident beam particles per beam monitor count. Appendix I describes the procedure for obtaining the ion chamber calibration factor K_{IC}. The number of counts per incident alpha in a telescope monitor M (M = M1, M2, or M3) for a given large target and for charge Q collected on the ion chamber capacitor is $M/(Q \cdot K_{IC})$. We may obtain the number of counts for the target material alone by subtracting off the same number for the corresponding empty target. The calibration factor for this monitor is the reciprocal of this number:

$$K_{LG} = \frac{K_{IC}}{\left(\frac{M}{Q}\right)_{LG} - \left(\frac{M}{Q}\right)_{LG\ EMPTY}} .$$

Then the calibration factor for a standard target of the same material is:

$$K_S = K_{LG} \cdot (\rho\ell)_S/(\rho\ell)_{LG}$$

where $\rho\ell$ is the target thickness in gm/cm^2. This calculation must be modified slightly for telsecope M3 because, as the target is moved vertically upward for measurement at a larger production angle θ, M3 also views the target at a larger production angle. This angular dependence is determined by fitting to the formula $M3/Q = a + b\theta + c\theta^2$ all the suitable data runs for a given beam energy and target. Then, if the large target calibration is made at production angle $\theta = 0°$, the M3 calibration factor is

$$K_S(\theta) = K_{LG}(0°) \cdot (1 + b\theta/a + c\theta^2/a)(\rho\ell)_S/(\rho\ell)_{LG} .$$

As a check on this procedure, the cross sections obtained were compared for different beam monitors, and the cross sections obtained using the large and standard targets and the small and thin C targets were compared and found to be in agreement within the assigned errors. The results of the calibrations for all three alpha particle beam energies on the carbon target are given in Table 3 in Section III, where the calibration factors given for M3 apply at production angle $\theta = 0°$.

APPENDIX III

Acceptance Calibration

We define the solid angle-momentum acceptance of the detectors and spectrometer as

$$\Delta\Omega \ \frac{\Delta p}{p_0} = \iiint \varepsilon(\theta_x, \theta_y, \frac{p}{p_0}) \ d\theta_x d\theta_y d\left(\frac{p}{p_0}\right) \qquad (1)$$

where p_0 is the spectrometer rigidity setting and θ_x, θ_y, and p are the horizontal and vertical production angles and the particle magnetic rigidity, respectively, at the target, and $\varepsilon(\theta_x, \theta_y, \frac{p}{p_0})$ is the probability (efficiency) for detecting such a particle.

During the design and construction of the spectrometer, the acceptance was predicted using the optical transforms from target to detectors calculated by program LBL TRANSPORT. To first order this is simply the dimensions of the detectors divided by the Jacobean determinant of the transformation

$$\Delta\Omega \ \frac{\Delta p}{p_0} = X_5 Y_5 X_4 / J\left(\frac{x_5, \ y_5, \ x_4}{\theta_x, \ \theta_y, \ \frac{p}{p_0}}\right) .$$

where X_5, Y_5, and X_4 are the detector sizes (at focus F4 and focus F5). Because there are second-order effects linking θ_x and p/p_0, a more exact calculation using the second order transforms generated by TRANSPORT was carried out, employing a complex but straightforward analytic integration giving the result $\Delta\Omega \ \frac{\Delta p}{p_0} = 9.35$ μsr.

The acceptance was also determined empirically by measuring the detection efficiency $\varepsilon(\theta_x, \theta_y, p/p_0)$ using primary beams deflected by small

angles θ_x and θ_y at the target. The efficiency $\varepsilon_x(\theta_x,0,p/p_0)$ as a function of horizontal angle and rigidity at $\theta_y = 0°$ was determined by mounting a small horizontal bending magnet M6S at the target which was used to deflect a 1.75 GeV/c/N proton beam through angles θ_x. Such a low momentum was needed because of the modest strength of the M6S magnet. Similarly, the efficiency $\varepsilon_y(0,\theta_y,p/p_0)$ was measured with the deflection provided by vertical bending magnets M6V and M7V located symmetrically upstream and downstream of the target. The 2.88 GeV/c/N alpha beam was used in this set of measurements to minimize the error in angle setting due to the difficulty in setting and controlling M6V and M7V at low currents. The rigidity dependence was determined by varying the spectrometer rigidity setting p_0. The incident beams were counted with a target-sized scintillation counter T2 mounted at the target position. The efficiency is then $\varepsilon(\theta_x,\theta_y,p/p_0) = \text{TRIGGERS}(\theta_x,\theta_y,p/p_0)/T2$ where, as defined in Section III, TRIGGERS = F4•F5X•F5Y. The results of the measurements are shown in Fig.A3 with hand-drawn curves to guide the eye. The fact that the maximum efficiency reached is $\varepsilon_{MAX} = 0.9$ may indicate obstructions or misalignment in the spectrometer beamline.

In order to determine the acceptance, it is necessary to perform the integration indicated in equation (1). For the integrand we used the following function, which is consistent with the horizontal and vertical measurements:

$$\varepsilon(\theta_x,\ \theta_y,\ p/p_0) = \frac{\varepsilon_x(\theta_x,\ 0,\ p/p_0)\varepsilon_y(0,\ \theta_y,\ p/p_0)}{\varepsilon_y(0,\ 0,\ p/p_0)}$$

with the denominator included so as not to double count the maximum

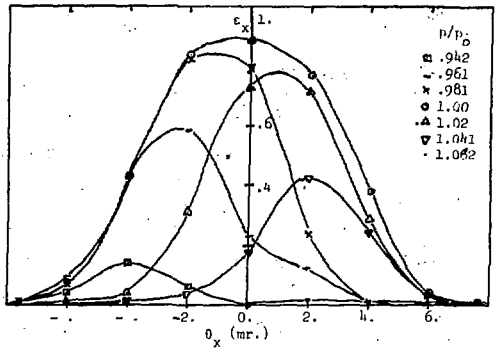

Fig.A3a $\epsilon_x(\theta_x, 0, \frac{p}{p_o})$ vs. θ_x 1.75 GeV/c PROTONS

CURVES ARE HAND DRAWN TO GUIDE THE EYE

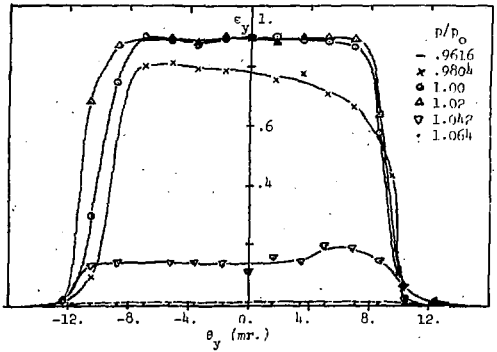

Fig. A3b $\epsilon_y(0, \theta_y, \frac{p}{p_o})$ vs. θ_y 2.88 GeV/c/N ALPHAS

XBL 779-2470

efficiency and the momentum dependence. The integration was performed by fitting a cubic to four consecutive points and integrating piecewise. As a check on this method the momentum dependence at $\theta_x = \theta_y = 0°$ was integrated over the independent measurements of $\epsilon_x(0, 0, p/p_0)$, using 1.75 GeV/c protons, and $\epsilon_y(0, 0, p/p_0)$, using 2.88 GeV/c/N alphas. The measured points are shown in Fig. A4 with hand-drawn curves. The points are not identical for the two measurements due to the greater spread of the lower energy beam. The results of the integrations differ by 3%.

The result of the integration of the solid angle-momentum acceptance is 7.81 μst, which differs from the predicted result $\epsilon_{MAX} \cdot 9.35 = 8.24$ μst by 5%. We have used this measured value with an assigned error of ±8%, which includes the effects of the uncertainty in the magnet settings and the measurement and integration procedure.

It was also necessary to determine the acceptances of the angle and momentum bins described in Section IV. The resolution in angle and momentum in the acceptance calibration measurements was only good enough to give an approximate set of results for these sub-acceptances. In order to get more precise results we measured cross sections using overlapping angle and momentum settings and divided up the total acceptance among the bins in order to obtain agreement in the overlapping regions. The results of this procedure are given in Table A1.

Regions in which the cross section is flat were used to determine the relative acceptances of the bins, and regions where the cross section is very steep were used to determine the mean angle or momentum for each bin. It was found that counters F5Y-5 and F5Y-4 had less acceptance than F5Y-1, 2, and 3. This result was consistent with the fact that $\epsilon_{MAX} = 0.9$,

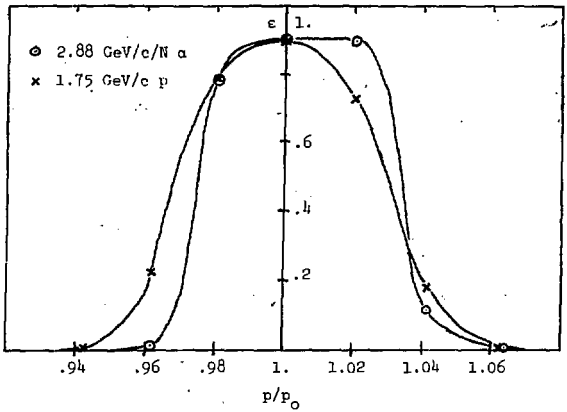

Fig.A4 $\varepsilon(0, 0, \frac{p}{p_o})$ vs. $\frac{p}{p_o}$

XBL 779-2471

Table A1

RESULTS OF ACCEPTANCE CALIBRATION

BIN	$\langle\theta\rangle$(mr.)	$\langle p/p_0 \rangle$	$\Delta\Omega\ \Delta p/p_0$ (μsr)
$\theta_y 1$	-7.6	1.0	1.614
$\theta_y 2$	-3.8	1.0	1.614
$\theta_y 3$	0	1.0	1.614
$\theta_y 4$	3.6	1.0	1.527
$\theta_y 5$	7.6	1.0	1.43
P1	0	0.029	2.170
P2	0	1.011	1.279
P3	0	1.0	1.537
P4	0	.987	1.178
P5	0	.968	1.721
Central	0	1.0	1.556
Whole	0	1.0	7.81

indicating a possible obstruction in the beamline and also consistent with the crude results of the acceptance calibration for these bins. The mean angle θ_y for these bins was adjusted by assuming the loss of acceptance was due to an obstruction which shadowed the lower portions of the counters, and this made the very sharp angular distributions smooth. Similarly the results obtained for the five momentum bins were consistent with the approximate results of the acceptance measurement and gave smooth momentum distributions in both flat and steep regions.